TAMPEREEN TEKNILLINEN YLIOPISTO
TAMPERE UNIVERSITY OF TECHNOLOGY

Muhammad Waqas Ahmad Khan

Inductively Powered Implantable System with Far-field Data Transmitter for an Intracranial Pressure Monitoring Application

Design and Performance Validation

Julkaisu 1552• Publication 1552

Tampere 2018

Tampereen teknillinen yliopisto. Julkaisu 1552
Tampere University of Technology. Publication 1552

Muhammad Waqas Ahmad Khan

Inductively Powered Implantable System with Far-field Data Transmitter for an Intracranial Pressure Monitoring Application

Design and Performance Validation

Thesis for the degree of Doctor of Science in Technology to be presented with due permission for public examination and criticism in Tietotalo Building, Auditorium TB104, at Tampere University of Technology, on the 7th of June 2018, at 12 noon.

Tampereen teknillinen yliopisto - Tampere University of Technology
Tampere 2018

Doctoral candidate: Muhammad Waqas Ahmad Khan
Wireless Identification and Sensing System (WISE)
Faculty of Biomedical Sciences and Engineering
Tampere University of Technology
Finland

Supervisor: Lauri Sydänheimo, Prof., Dr. Tech.
Wireless Identification and Sensing System (WISE)
Faculty of Biomedical Sciences and Engineering
Tampere University of Technology
Finland

Instructors: Leena Ukkonen, Prof., Dr. Tech.
Wireless Identification and Sensing System (WISE)
Faculty of Biomedical Sciences and Engineering
Tampere University of Technology
Finland

Toni Björninen, Dr. Tech
Wireless Identification and Sensing System (WISE)
Faculty of Biomedical Sciences and Engineering
Tampere University of Technology
Finland

Pre-examiners: Hendrik Rogier, Prof.
Department of Information Technology
University of Ghent
Belgium

Nuno Borges Carvalho, Prof.
Institute of Telecommunications
University of Aveiro
Portugal

Opponents: Raimo Sepponen, Prof., Dr. Tech
Department of Electrical Engineering and Automation
Aalto University
Finland

Ilkka Laakso, Assistant Professor
Electromagnetics in Health Technologies
Department of Electrical Engineering and Automation
Aalto University
Finland

ISBN 978-952-15-4152-0 (printed)
ISBN 978-952-15-4155-1 (PDF)
ISSN 1459-2045

Abstract

Monitoring of the intracranial pressure (ICP) is an essential activity for many brain diseases and injuries. For an adult, ICP value is between $7\ mmHg$ to $15\ mmHg$. However, for a critically ill patient, the ICP should be maintained below $20\ mmHg$. Therefore, continuous monitoring of ICP is a life-saving activity. Several invasive and non-invasive methods have been proposed for monitoring of the ICP. However, invasive methods cannot be used for continuous monitoring of the ICP due to the risk of infection. Moreover, non-invasive methods lack in accuracy.

Therefore, many researchers reported battery-powered or fully passive implantable systems. However, a battery-powered implant has limited life and large size. On the other hand, in a fully passive implant the readout distance is relatively small in comparison with a battery-powered implant due to its zero-power operation.

In contrast, this work presents the development of an inductively powered implantable system equipped with a data transmission unit for an ICP monitoring application. The developed system has three main parts: an implant or in-body unit, an on-body unit and an off-body unit. The on-body unit powers the implant through inductive near-field link. After the activation, the implant, consists of a piezoresistive pressure sensor and a data transmission unit, transmits the pressure signal at the industrial, scientific, and medical radio (ISM) band of $2.45\ GHz$. The off-body unit receives the transmitted signal from the implant and estimates the pressure value.

The simulation and the measurement results of both near-filed and far-field links are presented. After the development of the system, the pressue readout measurement results have been presented in the air, water and in a setting mimicking the human head dielectric properties. For biocompatibility, the implant is coated with biocompatible adhesive silicone. The effect of coating on both wireless links has also been studied.

Finally, this work also presents the effect of misalignment between the inductively coupled antennas on the pressure readout accuracy of the developed ICP monitoring system and discusses the solution to overcome this impact. The thesis also presents the response of the developed ICP monitoring system with the change in the temperature.

.

ACKNOWLEDGEMENT

This research has been carried out in Wireless Identification and Sensing System (WISE) research group, at the Department of Electronics and Communications Engineering until the end of 2016, and then at BioMediTech Institute and Faculty of Biomedical Sciences and Engineering at the Tampere University of Technology during the year 2017. This work is funded by the Finnish Funding Agency for Technology and Innovation (TEKES), the Academy of Finland and Jane and Aatos Erkko Foundation. The financial support awarded by Nokia Foundation and Tekniikan Edistämissäätiö Finland are gratefully acknowledged. I would like to thank Amphonel Advance Sensors for donating the P162 NovaSensor piezoresistive pressure sensor die for our initial research.

I would like to express my sincere gratitude to my supervisor Prof. Lauri Sydänheimo and advisor Prof. Leena Ukkonen. Without the precious support of Prof. Lauri Sydänheimo and Prof. Leena Ukkonen, my research work would have not progressed to this point. I especially want to thank my advisor Dr. Toni Björninen for his continuous and valuable feedback on my work. I would also like to thank Prof. Yahya Rahmat-Samii from the University of California for the great collaboration and his constructive feedback and insightful comments.

I would like to thank all of my friends and colleagues in the WISE research group. Their continuous support and collaboration help me to achieve this goal. I would like to express my deepest thanks to my parents and my wife for their continuous support to make this thesis possible.

Tampere April. 2017

Muhammad Waqas Ahmad Khan

Contents

List of Figures

List of Tables

List of Publications

I. **M. W. A. Khan**, T. Björninen, L. Sydänheimo, L. Ukkonen, “Characterization of two-turns external loop antenna with magnetic core for efficient wireless powering of cortical implants,” *IEEE Antennas Wireless Propag. Lett*., vol. 15, pp. 1410-1413, Apr. 2016.

II. **M. W. A. Khan**, T. Björninen, L. Sydänheimo, L. Ukkonen, “Remotely powered piezoresistive pressure sensor: toward wireless monitoring of intracranial pressure,” *IEEE Microw. Wireless Compon. Lett.,* vol. 26, no. 7, pp. 549–551, June 2016.

III. **M. W. A. Khan**, L. Sydänheimo, T. Björninen, L. Ukkonen, “Wirelessly powered implantable system for wireless long-term monitoring of intracranial pressure,” *IEEE International Workshop on Antenna Technology: Small Antennas, Innovative Structures, and Applications (iWAT*), pp. 122-124, 2017 .

IV. **M. W. A. Khan**, E. Moradi, L. Sydänheimo, T. Björninen, Y. Rahmat-Samii, L. Ukkonen, “Miniature co-planar implantable antenna on thin and flexible platform for fully wireless intracranial pressure monitoring system,” *Intl. J. Antennas Propag*., vol. 2017, Article ID 9161083, 9 pages, 2017.

V. **M. W. A. Khan**, L. Sydänheimo, L. Ukkonen, T. Björninen, “Inductively powered pressure sensing system integrating a far-field data transmitter for monitoring of intracranial pressure,” *IEEE Sensors J.*, vol. 17, no. 7, pp. 2191-2197, Apr. 2017.

VI. **M. W. A. Khan**, M. Rizwan, M. H.Behfar, L. Sydänheimo, T. Björninen, L. Ukkonen, “Effect of implant coating on wireless powering for intracranial pressure monitoring system,” *IEEE International Symposium on Antennas and Propagation (APS)*, pp. 389-390, July, 2017.

VII. **M. W. A. Khan**, M. Rizwan, L. Sydänheimo, Y. Rahmat-Samii, L. Ukkonen, T. Björninen, “Effect of temperature variation on remote pressure readout in wirelessly powered intracranial pressure monitoring system,” *IEEE Engineering in Medicine and Biology Society (EMBC)*, pp. 1728-1731, 2017.

VIII. **M. W. A. Khan**, M. Rizwan, L. Sydänheimo, T. Björninen, Y. Rahmat-Samii, L. Ukkonen, “Characterization of 3-D loop antenna to overcome the impact of small lateral misalignment in wirelessly powered intracranial pressure monitoring system,” *IEEE Trans. on Antennas and Propag.*, vol. 65, no. 12, pp. 7405-7410, Dec. 2017.

AUTHOR'S CONTRIBUTION

I. The author conducted the designing, simulation and measurement of the loop antennas. The author also wrote the publication text. Co-authors reviewed the text and provided feedback.

II. The author conducted the simulation. The author conducted the experiments and wrote the publication text. Co-authors reviewed the text and provided feedback.

III. The author conducted the simulation. The author conducted the experiments and wrote the publication text. Co-authors reviewed the text and provided feedback.

IV. The author designed the antenna and conducted the simulations. Author and E. Moradi performed the measurements. T. Björninen cooperated in writing the Introduction in the publication text. Otherwise, the author wrote the remaining publication text. The rest of the co-authors reviewed the text and provided feedback.

V. The author conducted the simulation. The author conducted the experiments and wrote the publication text. Co-authors reviewed the text and provided feedback.

VI. The author conducted the simulation. Author and M. Rizwan conducted the experiment. Author and M. H.Behfar performed the coating to the sensor. The author also wrote the publication text. Co-authors reviewed the text and provided feedback.

VII. The author conducted the simulations. The author and M. Rizwan conducted the experiments. Author and T. Björnine jointly wrote the publication text. Co-authors reviewed the text and provided feedback.

VIII. The author conducted the simulations. M. Rizwan printed the 3-D substrate. The author and M. Rizwan conducted the experiments. The author also wrote the publication text. Co-authors reviewed the text and provided feedback.

1 Introduction

The intracranial pressure (ICP) was first described by the Scottish anatomist Alexander Monro in 1783 [1]. According to him;

(i) The brain is enclosed in a non-expandable skull
(ii) The brain is incompressible
(iii) Therefore, it is essential that the volume of blood in the cranial cavity is constant
(iv) There must be a continuous outflow of venous blood from cranial cavity such that this makes room for continuous arterial supply.

Few years later, George Kellie supported Monro's observation through experiment [2] and known as "Monro-Kellie hypothesis" or "Monro-Kellie doctrine". However, both missed the presence of cerebralspinal fluid (CSF). Although, Flemish anatomist Vesaliu had described the fluid in sixteen century, however, French physiologist Magendie proved it through animal experiment in 1842 [3]. In 1846, George Burrows introduced CSF as a factor in the "Monro-Kellie doctrine" [4].

According to the Monro-Kellie doctrine, cerebral spinal fluid (CSF), blood, and brain are all incompressible and are in volume equilibrium [5-7]. An increase in the volume of one component will result in the decrease in the volume of one or both of the other components. This means that volume of all components must remain constant for constant ICP. The relation between the intracranial pressure and the volume can be described as a pressure-volume curve. Figure 1 presents the relation between the intracranial pressure and the volume. Due to the compensatory reserve, the ICP do not vary much in the first part of the curve. After exceeding the compensatory reserve, there is rapid raise in the ICP. Raised ICP leads to a serious medical condition known as intracranial hypertension (IH). This could reduce the cerebral blood flow (CBF) and can cause ischemia and infarction.

Although normal ICP range varies with age, however, in adults, normal ICP is between $7\ mmHg$ to $15\ mmHg$. Sustained IH can damage the brain or even cause of death. Therefore, continuous monitoring of the ICP or management of the IH is critical. ICP can increase due to diverse causes which can be categorized as the intracranial, extracranial or postoperative complications of neuro-surgery [5-8].

ICP is commonly monitored through catheter inserted into the ventricular system. This method is accurate and allows on-site re-calibration and as well as the drainage of the CSF for IH management. Therefore, it is considered as a gold standard. However, due to its invasiveness, it has the risk of infection and haemorrhage. As a result, it cannot be used for repeated or prolonged use. Long-term monitoring of the ICP is a life-saving activity for patient suffering from IH due to an illness [5][6][9-10][13]. Due to the limitations of the invasive methods, non-invasive methods have been studied in recent literatures [11-12] for long-term monitoring of the ICP. However, non-invasive methods lack in the accuracy and due to anatomical variations, they cannot be used as a counter part of the invasive methods [13].

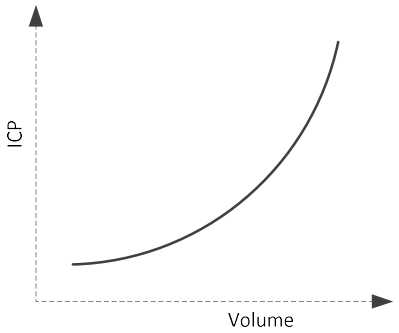

Figure 1: Relation between the intracranial pressure and the volume.

In the recent literatures, researchers have focused on the development of implantable systems for ICP monitoring. In an implantable system, an implant monitors the ICP and transmits it outside the skull. Researchers have either proposed a battery assisted implant [14] or a fully passive implant [15-17] for monitoring of the ICP. Battery assisted implants are large in size due to the size of the battery and have limited life due to the life of the battery. Fully passive implants have small read range due to their zero-power operation.

1.1 Scope of the thesis

This work is focused on the development of an inductively powered implantable system with a far-field data transmitter for monitoring of the ICP. Figure 2 shows the system-level description of the developed system for monitoring of the ICP. The developed system has three main parts. First is an implant or an in-body unit which monitors the pressure and transmits it outside the skull through a far-field link. Second is an on-body unit which powers the implant through inductive near-field link. Third is an off-body unit which receives the transmitted signal from the implant. It is important to mention that the terms “implant” or “in-body unit” are interchangeably used throughout the thesis.

The system has two wireless links: near-field and far-field, as shown in Figure 2. The optimization of the near-field link is important for sufficient power transmission to activate the implant. The antenna designing for both implant and on-body unit is discussed for maximum link power efficiency in a human head model. In an inductive near-field link, maximum power transfer efficiency between the antennas depends on their size, structure, separation, material properties and alignment between them [18].

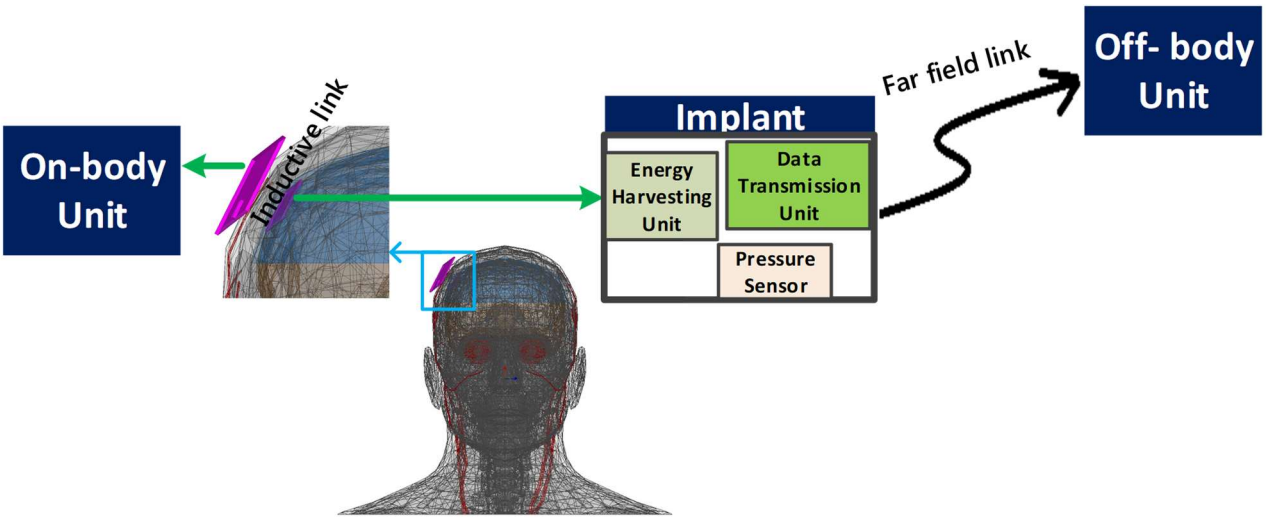

Figure 2. The system-level description of the developed system for monitoring of the ICP

Due to the nature of the application, the implant antenna should be as small as possible. Similarly, the antenna of the on-body unit should also be light-weight and small in size. Maximum power transmission from the antenna of an on-body unit is limited by the human safety limit known as specific absorption rate (SAR). This work follows U.S. federal communications commission (FCC) regulation which limits the SAR averaged over one gram of tissue to $SAR_{max} = 1.6\, W/kg$. However, the SAR limit recommended by The Council of the European Union is $SAR_{max} = 2\, W/kg$ averaged over 10 grams of tissue. Different structures of the antenna are studied for maximum power transmission without sacrificing the maximum link power efficiency. For a small loop antenna, the near-field radiated power density is inductive in nature. Near magnetic field in a small loop antenna can be enhanced by increasing the number of turns or by inserting the ferrite core with high permeability within the circumference or perimeter of the loop antenna [19]. Therefore, 2-D and 3-D loop antenna structures are studied in an on-body unit for efficient wireless powering. The maximum power transfer efficiency decreases as the separation between the coupled antennas increases due to the decrease of the coupling. For a fix implant, if antenna of the on-body unit is brought close to the skin surface then maximum link power efficiency increases due to decrease in the separation between the coupled antennas. However, due to SAR limitation, it decreases the maximum allowed power transmission from the antenna of the on-body unit. The goal is to find an optimum distance from the skin that results in a maximum power at the implant. Therefore, the separation between the antenna of the on-body unit and the skin is studied based on the available power at the implant

terminals. Human tissues presence between the inductively coupled antennas exert excessive loss. Simple and accurate modelling of the human head is important for simulating the inductive near-field link. Detailed and complex human head models are accurate but require more time and computation power for simulation. A comparison is done between the tissue-layer and the anatomical human head model provided by ANSYS HFSS v15. A small misalignment between strongly coupled antennas significantly decreases the voltage at the implant terminals. It is important that coupled antennas should tolerate the small misalignment without significat affect on the voltage at the implant terminals. A 3-D loop antenna structure for an on-body unit helps to overcome the impact of the small misalignment between coupled antennas.

In this work, an energy harvesting unit activates the implant by converting the radio frequency (RF) to direct current (DC) voltage. A piezoresistive pressure sensor in the implant monitors the pressure. A data transmission unit consists of an amplifier and a voltage controlled oscillator (VCO) transmits the pressure signal at the industrial, scientific, and medical radio (ISM) band of $2.45\ GHz$. The output of the VCO is connected to a far-field antenna. The implant is designed on a thin and flexible substrate. Due to small available space, far-field antenna design is critical. Although researchers have reported several far-field implant antenna miniaturization techniques [20-38], however, co-planar far-field antenna structure is proposed due to small available space and thin substrate. The optimization and designing of the far-field implant antenna are discussed in detail.

The transmitted signal from the implant is received by an off-body unit. In a piezoresistive pressure sensor, the output voltage of the sensor is sensitive towards the change in the pressure. The implant is developed and tested in three main stages. At the first stage, the implant does not contain data transmission unit and the response of the implant is analyzed in the air by monitoring the output voltage of the pressure sensor. At the sencond stage, the response of the implant is verified in the liquid (water) without a data transmission unit by monitoring the output voltage of the pressure sensor. At the third stage, a data transmission unit is included in the final design of the implant and the response of the implant is verified in a setting mimicking the dielectric properties of the human head.

For biomedical application, the implant should either be made of biocompatible materials or coated with biocompatible materials. This work also presents the effect of the implant coating material on both near-field and far-field links. Moreover, the response of the system is also discussed due to the change in the tempereature.

1.2 Structure of the thesis

This thesis is organized in six chapters (see Figure 3). Chapter 1 provides the literature review of the intracranial pressure (ICP) and highlights the main objectives of the thesis. Chapter 2 describes the antenna fundamentals, theoretical background of an inductive near-field link and far-field antenna

design considerations. Chapter 3 presents the simulation and measurement results of the developed ICP monitoring system without a data transmission unit. An ICP monitoring system with a data transmission unit is presented in Chapter 4. The effect of misalignemnt between the coupled antennas and tempereture are discussed in Chapter 5. Finally, thesis conclusion and future trends are presented in Chapter 6.

1. Introduction	• Literature review of the ICP • Thesis objectives
2. Threoretical Background	• Antenna fundamentals • Inductive near-field link theory • Far-field antenna design considerations
3. Intracranial pressure monitoring system without a data transmission unit	• Design of an on-body unit antenna [I] • Pressure measurement in the air [II] • Pressure measurement in the liquid (water) [III]
4. Intracranial pressure monitoring system with a data transmission unit	• Far-field antenna design [IV] • Pressure measurement in a setting mimicking the human head environment [V] • Effect of the coating on wireless links [IV, VI]
5. Effect of misalignment between inductively coupled antennas and temperature on the performance of the intracranial pressure monitoring system	• Effect of misalignment between inductively coupled antennas on the system performance [VIII] • Effect of temperature on the system performance [VII]
6. Conclusion	• Summary of the thesis • Future trends

Figure 3. Structure of the thesis

2 Theoretical Background

The implant is powered through an inductive near-field link. In an inductive near-field link, the primary coil (in our case on-body antenna) transmits the power inductively across the tissues of the human head to the secondary coil (in our case implant antenna). The received power is then rectified and activates the implant circuitry. After the activation, a pressure sensor monitors the pressure and a data transmission unit transmits the pressure outside the skull through a far-field antenna. This chapter discusses the antenna fundamentals, theoretical background of an inductive near-field link and far-field antenna design considerations for an implant.

2.1 Antenna fundamentals

An antenna can be defined in simple words as a transitional structure between free-space and a guiding device [19]. It is an essential element in any wireless communication system. Antenna performance can be described through various parameters. However, it is not necessary to specify all of the parameters for a complete description of an antenna because some of them are interrelated [19]. In this section, we will focuse only a few antenna parameters which are going to be used in the coming chapters.

Antenna surrounding can be sub-divided into two main regions including near-field and far-field. Close to an antenna, it has both reactive and radiative energies and as a result the field pattern of the antenna changes rapidly with distance. However, as we move away from the antenna, reactive energy becomes negligible whereas radiative energy starts dominating. These regions can be separated by radius *R* as shown in Figure 4 and given by [39]

$$R = \frac{2D^2}{\lambda} \quad \text{[m]} \qquad (2.1)$$

where D is the diameter of the antenna or the largest dimension of the antenna (m) and λ is the wavelength (m). The near-field region can be defined as the region within the *R,* whereas the region beyond the *R* is the far-field region. Equation (2.1) defines the near-far field regions for electrically large antennas. However, in this work, we present electrically small antennas. Therefore, for electrically small antennas, the R is given as $R = \frac{\lambda}{2\pi}$.

Antenna total efficiency takes into account the mismatch efficiency and radiation efficiency and is given as [19]

$$e_0 = e_r e_{cd} \quad \text{[dimensionless]} \qquad (2.2)$$

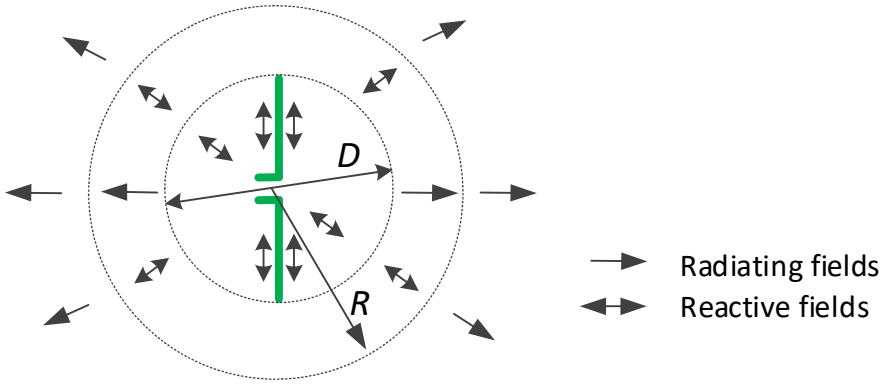

Figure 4. Definition of antenna field regions [39]

where e_0 is antenna total efficiency, $e_r = (1 - |\Gamma|^2)$ is mismatch efficiency at antenna input terminals and e_{cd} is antenna radiation efficiency. Γ is defined as voltage reflection coefficient at the input terminals of the antenna and is given as [19]

$$\Gamma = \frac{Z_i - Z_o}{Z_i + Z_o} \qquad \text{[dimensionless]} \quad (2.3)$$

where Z_i is the input impedance of the antenna and Z_o is the characteristic impedance of the transmission line.

Directivity of an antenna can be defined as the radiation intensity in a specific direction to the radiation intensity averaged over all directions [19]. Gain of the antenna is another important parameter. It can be defined as the ratio of radiation intensity in a specific direction to the radiation intensity in the same direction if the antenna radiates isotropically. Gain can be calculated by multiplying the radiation efficiency to the directivity of the antenna and is given as

$$Gain = e_{cd} \times directivity \qquad \text{[dimensionless]} \quad (2.4)$$

If in equation (2.4), radiation efficiency is replaced by antenna total efficiency then it is called *absolute gain*.

In free space, for wireless communication system, it is important to explain Friis transmission formula. Assume a wireless communication system, as shown in Figure 5, has two antennas A and B which have gains G_A and G_B respectively, separated by distance L and arranged such that their reflection and polarization are matched. If antenna A is fed with power P_A, then power P_B received by antenna B is given as [19]

$$P_B = P_A G_A G_B \left(\frac{\lambda}{4\pi L}\right)^2 \qquad \text{[W]} \quad (2.5)$$

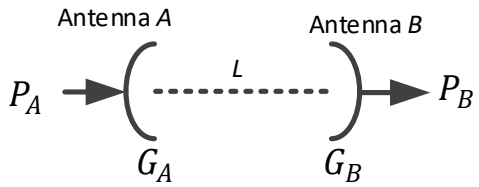

Figure 5. A simple wireless communication system

2.2 Wireless powering through an inductive near-field link

Loop antennas are simple in structure and inexpensive. They can have different shapes such as circular or rectangular. If the circumference of a loop antenna is less than one-tenth of the wavelength then the loop antenna is considered as an electrically small antenna. Due to the small size of an electrically small antenna, its effective area or effective aperture is small and therefore these antennas are low efficient. However, if the circumference of the loop antenna approaches to the wavelength then this is known as an electrically large antenna. This section discusses the electrically small antenna.

2.2.1 Analysis of an electrically small loop antenna

Figure 6 shows a circular loop antenna with radius a on the *x-y* plane of a polar coordinate system with $z = 0$. With the assumption that wire of the loop is thin and current has uniform distribution, the current spatial distribution I_ϕ along the wire for an electrically small antenna is given as [19]

$$I_\phi = I_o \quad \text{[A]} \qquad (2.6)$$

where $I_o$is a constant. Magnetic vector potential $\boldsymbol{A}$ helps to determine the electromagnetic field produced by I_o at a distance r from the loop center point and is given as [19]

$$\boldsymbol{A} = \boldsymbol{a_\phi} \frac{a^2 \mu I_o}{4} e^{-jkr} sin\theta \left[\frac{jk}{r} + \frac{1}{r^2}\right] \quad \text{[V.s.m}^{-1}\text{]} \qquad (2.7)$$

where μ is the permeability of the medium (H/m) and k is wave number and is given as

$$k = \omega\sqrt{\mu\varepsilon} = \frac{\omega}{c} = \frac{2\pi f}{c} \quad \text{[rad/m]} \qquad (2.8)$$

where ω is angular frequency (rad/m), f is frequency (Hz) of the electromagnetic wave and c is the speed of electromagnetic wave in the medium (m/s). It is important to note that $\boldsymbol{A}$ has only ϕ-component whereas its r- and θ-components are zero. The relation between magnetic flux density $\boldsymbol{B}$ and magnetic field intensity $\boldsymbol{H}$ is given as

$$\boldsymbol{B} = \mu \boldsymbol{H} \qquad \text{[Wb/m}^2\text{ or Tesla]} \qquad (2.9)$$

$\boldsymbol{B}$ can also be expressed as the curl of $\boldsymbol{A}$

$$\boldsymbol{B} = \boldsymbol{\nabla} \times \boldsymbol{A} \qquad (2.10)$$

Substituting the value of $\boldsymbol{B}$ from (2.9) into (2.10), $\boldsymbol{H}$ can be expressed as the curl of $\boldsymbol{A}$

$$\boldsymbol{H} = \frac{1}{\mu} \boldsymbol{\nabla} \times \boldsymbol{A} \qquad \text{[A/m]} \qquad (2.11)$$

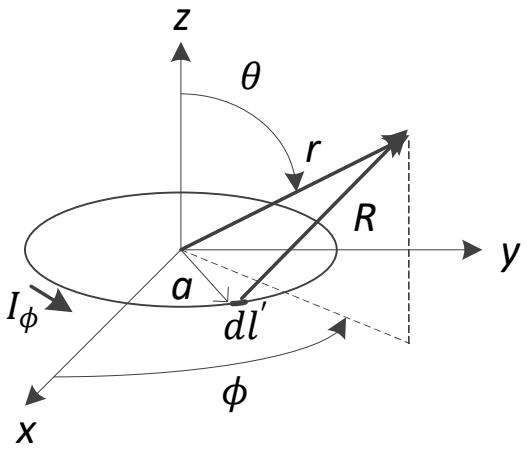

Figure 6. Geometrical arrangement for an electrically small circular loop analysis

Substituting the value of $\boldsymbol{A}$ from (2.7) into (2.11) and solving (2.11) would provide the magnetic field components of an electrically small circular loop as following [19]

$$H_r = j\,\frac{ka^2 I_o}{2r^2} e^{-jkr} cos\theta \left[1 + \frac{1}{jkr}\right] \qquad (2.12)$$

$$H_\theta = -\frac{(ka)^2 I_o}{4r} e^{-jkr} sin\theta \left[1 + \frac{1}{jkr} + \frac{1}{(jkr)^2}\right] \qquad (2.13)$$

$$H_\phi = 0 \qquad (2.14)$$

Electric field $\boldsymbol{E}$ can be computed through the curl of magnetic field $\boldsymbol{H}$

$$\boldsymbol{E} = \frac{1}{j\omega\varepsilon_o} \boldsymbol{\nabla} \times \boldsymbol{H} \qquad \text{[V/m]} \qquad (2.15)$$

Similarly, electric field components for an electrically small loop antenna geometry in Figure 6 can be given as [19]

$$E_r = E_\theta = 0 \tag{2.16}$$

$$E_\phi = \eta \frac{(ka)^2 I_o}{4r} e^{-jkr} sin\theta \left[1 + \frac{1}{jkr}\right] \tag{2.17}$$

where $\eta = \sqrt{\frac{\mu}{\varepsilon}}$ is intrinsic wave impedance of the media. For free space it is equal to $377\ \Omega$.

From equations (2.12) to (2.17), for an electrically small loop antenna, we can conclude as following:

In near-field region ($\boldsymbol{kr \ll 1}$): for magnetic field both H_r and H_θ exist. However, for electric field only $E_\phi$exists.

In far-field region ($\boldsymbol{kr \gg 1}$): for magnetic field $H_r \to 0$ and only H_θ left. However, for electric field only E_ϕ exists.

Complex power density for an electrically small loop antenna of Figure 6 is given as [19]

$$\boldsymbol{W} = \frac{1}{2}(\boldsymbol{E} \times \boldsymbol{H}^*) = \frac{1}{2}(-\boldsymbol{a_r} E_\phi H_\theta^* + \boldsymbol{a_\theta} E_\phi H_r^*) \qquad [\text{W/m}^2] \tag{2.18}$$

where asterisk marks complex conjugate. If (2.18) is integrated over a closed surface, the radial complex power P_r can be obtained as following [19]

$$P_r = \eta \frac{\pi}{12} (ka)^4 I_o^2 \left[1 + j \frac{1}{kr^3}\right] \qquad [\text{W}] \tag{2.19}$$

From (2.19), we can conclude that:

In near-field region ($\boldsymbol{kr \ll 1}$): $\frac{1}{kr^3} \gg 1$ and therefore, P_r is mainly reactive.

In far-field region ($\boldsymbol{kr \gg 1}$): $\frac{1}{kr^3} \ll 1$ and therefore, P_r is mainly real.

Another important point to note is that radial power for an electrically small loop antenna in the near-field is inductive in nature, however, for electrically small dipole it is capacitive in nature. [19]

2.2.2 Inductive near-field link theory

Consider a loop system shown in Figure 7(a) in which two loops or coils are in each other vicinity and are perfectly aligned. The magnetic flux Φ_{12} produced due to i_1 in the first loop passes through the second loop. This results in an inductive near-field link. Coupling factor k_c and mutual inductance M are two parameters characterize the inductive near-field link strength and both are related as following [40]

$$M = k_c \sqrt{L_1 L_2} \qquad [\text{H}] \tag{2.20}$$

where L_1 and L_2 are the self-inductances of the first and the second loops respectively. The mutual inductance of the system shown in Figure 7(a) can be approximated as [40]

$$M = \mu N_1 N_2 \frac{\pi(a_1 a_2)^2}{2(r^2+a_1^2)^{\frac{3}{2}}} \tag{2.21}$$

where $N_1$and N_2 are the number of turns of the first and the second loops respectively. a_1 and a_2 are the radius of the first and the second loops respectively and r is the separation between the loops. From (2.21) we can conclude:

(i) If $a_1 > a_2$ then system is robust towards the misalignment between the loops.
(ii) If $a_1 = a_2$ then system has the highest mutual inductance.
(iii) Loops with larger radiuses result in the higher mutual inductance.

From [40], coupling factor k_c can be given as

$$k_c = \frac{\pi}{\sqrt[2]{\ln\left(\frac{a_1}{d_1}\right)\ln\left(\frac{a_2}{d_2}\right)}}\left(\frac{a_1 a_2}{r^2+a_1^2}\right)^{\frac{3}{2}} \tag{2.22}$$

Where d_1 and d_2 are the diameters of the first and the second loops respectively. Coupling factor k_c depends on the geometry of the loops or coils and separation between them. However, it is independent of the number of turns of the loops or coils.

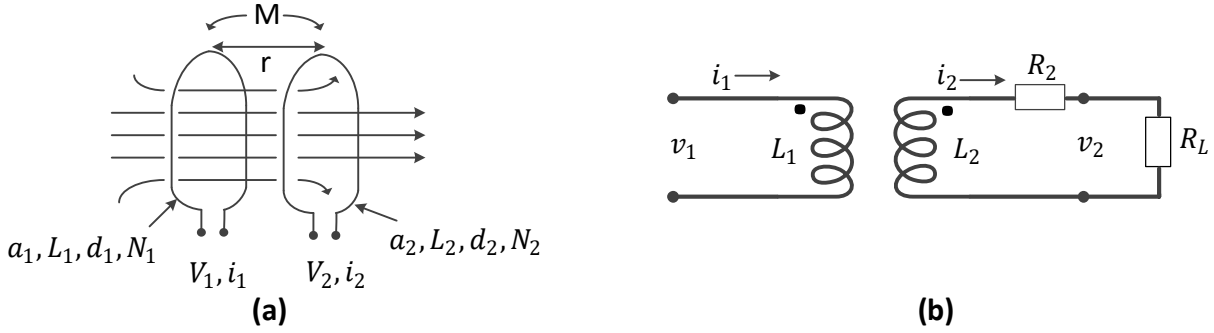

Figure 7. (a) Magnetically coupled circular loops (b) equivalent circuit diagram of coupled loops

According to Faraday's Law, if $i_1$changes then this changes the magnetic flux through the second loop and induces voltage v_2 in the second loop. If second loop is connected to the load R_L then the equivalent circuit diagram for coupled loops is shown in Figure 7(b). R_2 represents the ohmic losses in the second loop. The induced voltage v_2 across the load $R_L$can be given as [40]

$$v_2 = \frac{j\omega M.i_1}{1+\frac{j\omega L_2+R_2}{R_L}} \quad [\text{V}] \tag{2.23}$$

From (2.23) it is clear that load resistance R_L value has significant impact on the achieved voltage across the load R_L. For $R_L \rightarrow \infty,\ v_2 = j\omega M.i_1$. However, when $R_L \rightarrow 0$, $v_2 = 0$.

2.2.3 Modelling of an inductive near-field link

An inductive near-field link can be modelled as linear two-port network parameters $(Z, Y, S, or\ ABCD)$. In a linear two-port network, power analysis can be done through transducer gain G_t and maximum available power gain $G_{p,max}$ [41]. G_t can be defined as the ratio of the power delivered to the load to the available power from the source. G_t can be expressed in terms of the Z-parameters as following [41]

$$G_t = \frac{4R_S R_L |z_{21}|^2}{|(z_{11}+Z_S)(z_{22}+Z_L)-z_{12}z_{21}|^2} \quad \text{[dimensionless]} \quad (2.24)$$

where Z_S and $Z_L$are the source and load impedances respectively. R_L and R_S are the real parts of Z_L and Z_S respectively. Under unconditional stability, maximum available power gain $G_{p,max}$ is the maximum of G_t and is given as [41]

$$G_{p,max} = \frac{|Z_{21}|^2}{S+\sqrt{S^2-|Z_{12}Z_{21}|^2}} \quad \text{[dimensionless]} \quad (2.25)$$

where $S = 2Re(Z_{11})Re(Z_{22}) - Re(Z_{12}Z_{21})$. In an inductive near-field link, $G_{p,max}$ is maximum link power efficiency. In this work, inductive near-field link is optimized based on $G_{p,max}$.

2.3 Far-field implant antenna design considerations

Miniaturizing the overall size and exact form-factor to minimize the intrusiveness are the fundamental challenges in the design of a far-field implant antenna. Several techniques have been reported in the literature for implant antenna miniaturization and can be summarized as following:

(i) Using of high permittivity dielectric materials as substrate [20-22].
(ii) Using meandering/spiraling and/or inserting the slot/line to lengthen the current path on the radiating patch of the antenna [23-27]
(iii) Using a planar inverted-F antenna configuration [28-31]
(iv) Vertically stacking two or more radiating patches [32-34] and
(v) Loading (inductive, capacitive or split ring) for impedance matching [35-38].

To minimize the intrusiveness, the substrate thickness and rigidness are important. The goal is to use flexible and thin substrate. Recently, there have been reports of many implant antennas on the flexible substrate [42-47].

Usually, due to the small size of the implant, there is limited space available for an implant antenna. The two-sided structure of an implant antenna on thin substrate would result in a very narrow bandwidth of the antenna [19]. Two-sided structure means that a radiating patch is on the one side of the substrate and a ground is on the other side of the substrate. Moreover, due to other electronics in the implant, usually it is hard to find suitable space for a two-sided structure of an implant antenna. Therefore, an alternative is a co-planar implant antenna structure. In a co-planar structure, both the radiating patch and the ground are one the same side of the substrate. There has also been reported literature on a co-planar implant antenna structure [22][48-49].

3 Intracranial pressure monitoring system without a data transmission unit

This chapter discusses the development of an intracranial pressure (ICP) monitoring system without a data transmission unit. In the absence of the data transmission unit, the change in the pressure is monitored by monitoring the output voltage of the piezoresistive pressure sensor. Moreover, the system response is measured in the air and in the liquid (water). The simulation and measurement results of the inductive near-field link are discussed in detail.

3.1 Modelling of the inductive near-field link for wireless powering

Inductive near-field powering is used to power the implant. The implant is placed under the skull and the antenna of the on-body unit is placed at $5\ mm$ from the skin. The reason of $5\ mm$ distance from the skin is discussed in the coming section. Total distance between the implant and the antenna of the on-body unit is $16\ mm$. As explained in Section 2.2.1, near-field of an electrically small loop antenna in inductive in nature. Therefore, we have selected electrically small loop/coil antennas for wireless inductive powering. Tissue-layer model present in [50] is used to model the human head. Moreover, each tissue layer is assigned properties based on [51]. ANSYS HFSS v15 is used for simulation.

The maximum allowed power transmission $P_{t,max}$ is limited by the human safety limit known as specific absorption rate (SAR). In this work, we have followed the U.S. FCC regulation which limits the SAR averaged over $1-gram$ of tissue to $SAR_{max} = 1.6\ W/kg$. To activate an implant, we need to meet the voltage threshold that requires specific amount of power. Under conjugate matched condition, the maximum power received P_L by an implant load is given as: $P_L = P_{t,max} \times G_{p,max}$. This indicates that the goal is to maximize both $P_{t,max}$ and $G_{p,max}$ in an inductive near-field link. It is also important to note that $G_{p,max}$ depends on both the implant and the on-body unit antennas, however, $P_{t,max}$ depends only on the antenna of the on-body unit.

3.1.1 2-turns loop antenna for an on-body unit

Study of [Publication I] concludes that a 2-turns loop antenna can transmit more power without violating the SAR_{max} limit with the same size and dimensions compared to the single turn loop antenna (see Figure 8(a)). In a 2-turns loop antenna, there are two loops in series. First loop is on the front side of the substrate and the second loop is on the backside of the substrate as shown in Figure 8 (b-c). Due to the structural property of the 2-turns loop antenna, one feeding port of the antenna is away from the skin compared to the other. Therefore, it has only one E-field potential peak and

resulted in low and uniform SAR distribution compared to the single turn loop antenna as shown in Figure 9.

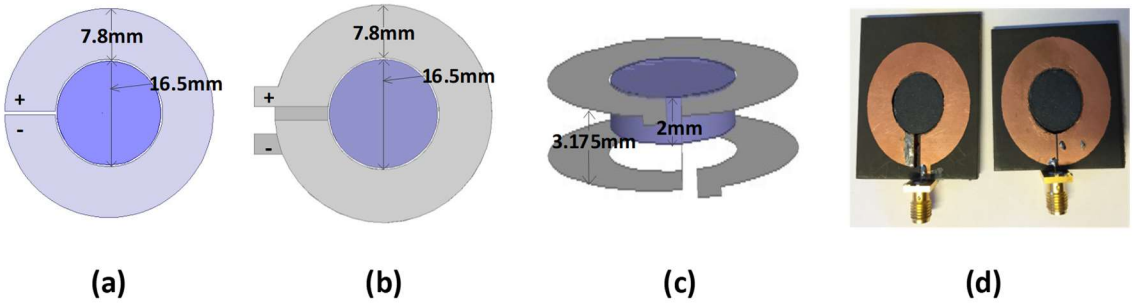

Figure 8. (a) Single turn loop antenna (b) the top view of 2-turns loop antenna (c) the side view of 2-turns loop antenna (d) fabricated single and 2-turns loop antennas [Publication I]

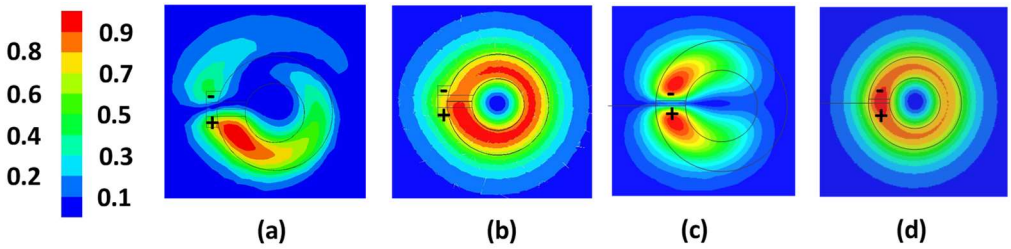

Figure 9. (a) Normalized E-field distribution for 2-turns loop antenna (b) normalized local SAR distribution for 2-turns loop antenna (c) normalized E-field distribution for single turn loop antenna (d) normalized local SAR distribution for single turn loop antenna at 100 MHz. [Publication I]

Simulation results from [Publication I] also shows that the distance of an antenna of the on-body unit from the skin has broad optimum. The optimum distance from the skin is studied based on the maximum received power P_L at the implant terminals. If an implant is considered fixed under the skull and distance between the antenna of the on-body unit and the skin is varied then with the decrease of distance $G_{p,max}$ increases, however, $P_{t,max}$ decreases due to increase in SAR and vice versa. The simulation [Publication I] results show that the implant would receive approximately the same amount of power if the distance of the on-body antenna from the skin varies from $5\ mm$ to $11\ mm$. Therefore, throughout this work, we kept the on-body antenna at $5\ mm$ from the skin in the development of the ICP monitoring system.

3.1.2 2-turns coil antenna for an implant

The implant is designed on a flexible polyimide substrate which has dielectric constant (ϵ_r) of 3.3 and tangent loss ($tan\delta$) of 0.002. The substrate has the thickness of $50\ \mu m$. For powering the implant, a 2-turns coil antenna is designed as shown in the Figure 10 (a). The implant front side (facing towards the on-body unit) has a 2-turns coil antenna and the implant backside has copper traces for

pressure sensor and other electronic components attachment. Our goal is to keep the implant's maximum dimensions to $2\ cm\ \times 2\ cm$. Therefore, the inner diameter of the 2-turns coil antenna is kept $11.2\ mm$, however, the thickness of the loop and separation between the loops of the coil are optimized for maximum $G_{p,max}$. The optimum values for the thickness of the loop and the separation between the loops are $0.26\ mm$ and $0.32\ mm$ respectively. [Publication II]

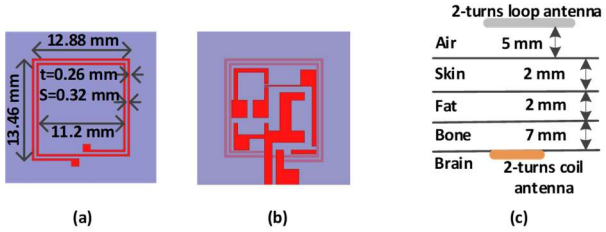

Figure 10. (a) The implant front side containing the 2-turns coil antenna (b) the implant backside for sensor and other electronics attachment (c) tissue-layer model of human head for simulation. [Publication II]

3.1.3 Simulation and measurement results of the inductive near-field link

The tissue-layer model shown in Figure 10 (c) is used for simulating the inductive near-field link. In the simulation, there is no coating material used around the implant. The effect of the coating material will be discussed in the next chapter. The 2-turns loop antenna of the on-body unit is designed on FR4 substrate with the height of $1.6\ mm$, the inner diameter of $16.5\ mm$ and the thickness of $7.8\ mm$. Figure 11 shows the simulated maximum link power efficiency $G_{p,max}$, the simulated maximum power transmission $P_{t,max}$ and maximum received power P_L at the implant. The optimum frequency for maximum $G_{p,max}$ is $6\ MHz$. With the increase in the frequency, $G_{p,max}$ decreases relatively slowly. However, $P_{t,max}$ and P_L decrease relatively fast.

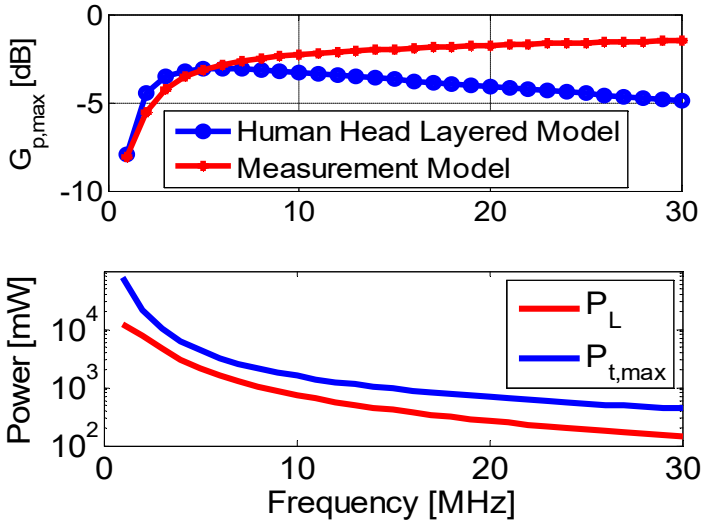

Figure 11. Simulated $G_{p,max}$, $P_{t,max}$ and P_L[Publication II].

After fabrication, an LC-matching network is used for the 2-turns loop antenna of the on-body unit to match it to $50\ \Omega$. However, a capacitor in a parallel configuration is used as a matching network for the 2-turns coil antenna of the implant. An LC-matching network is sensitive towards the capacitor and the inductor values. Therefore, we are able to match them at $11\ MHz$ instead of $6\ MHz$. However, simulated $G_{p,max}$ at $11\ MHz$ and $6\ MHz$ are within $1\ dB$ difference. [Publication II]

At low frequency, losses due to the tissue layers are low. Therefore, to make the measurement simple, an air gap of $16\ mm$ between the coupled antennas can be used instead of the tissue layers. As shown in Figure 11, the difference in $G_{p,max}$ for measurement and tissue-layer models is only $1.21\ dB$ at $11\ MHz$. The measured S-parameters of the inductive link at $11\ MHz$ are $S11 = -4.3\ dB$, $S22 = -24.8\ dB$ and $S12 = S21 = -15.5\ dB$. The simulated and the estimated $G_{p,max}$ are $-2.17\ dB$ and $-3.55\ dB$ respectively. The transmission loss is high due to the parasitics of the inductor and the capacitors in the matching networks. [Publication II]

3.2 Pressure readout experiment in the air

A rectifier in the implant converts the RF-to-DC. Rectifier has two Schottky diodes (Skyworks SMS7630 series) for rectification and two $1\ \mu F$ capacitors in the charge pump configuration. Initially, Amphenol P162 NovaSensor piezoresistive pressure sensor die is used as a pressure monitoring sensor. It has overall dimensions of $1150\mu m \times 725\mu m \times 170\mu m$. Moreover, it is a half bridge configuration and requires two $800\ \Omega$ external resistors to complete the full bridge. The measured full bridge input resistance of the sensor is $795\ \Omega$ [Publication II].

Figure 12 (a) shows the measurement setup. The implant is placed inside of an air-sealed plastic container and the antenna of the on-body unit is placed outside the container. The airflow is controlled through an in/out airflow valve and a reference pressure monitoring device (IMF electronic gmbh PA 3528) is also connected. The pressure change is monitored by monitoring the output voltage of the sensor.

After the measurement setup, an input power of $23.98\ dBm$ ($250\ mW$) is fed to the antenna of the on-body unit. The pressure sensor needs a minimum of $1\ V$ at its input terminals for activation. However, with $23.98\ dBm$ input power, the achieved voltage is $1.894\ V$ at the input terminals of the sensor. This means that overall system power transfer efficiency is $1.8\ \%$ [Publication II]. Figure 12 (b) shows the measured power flow of the developed ICP monitoring system in the air without a data transmission unit.

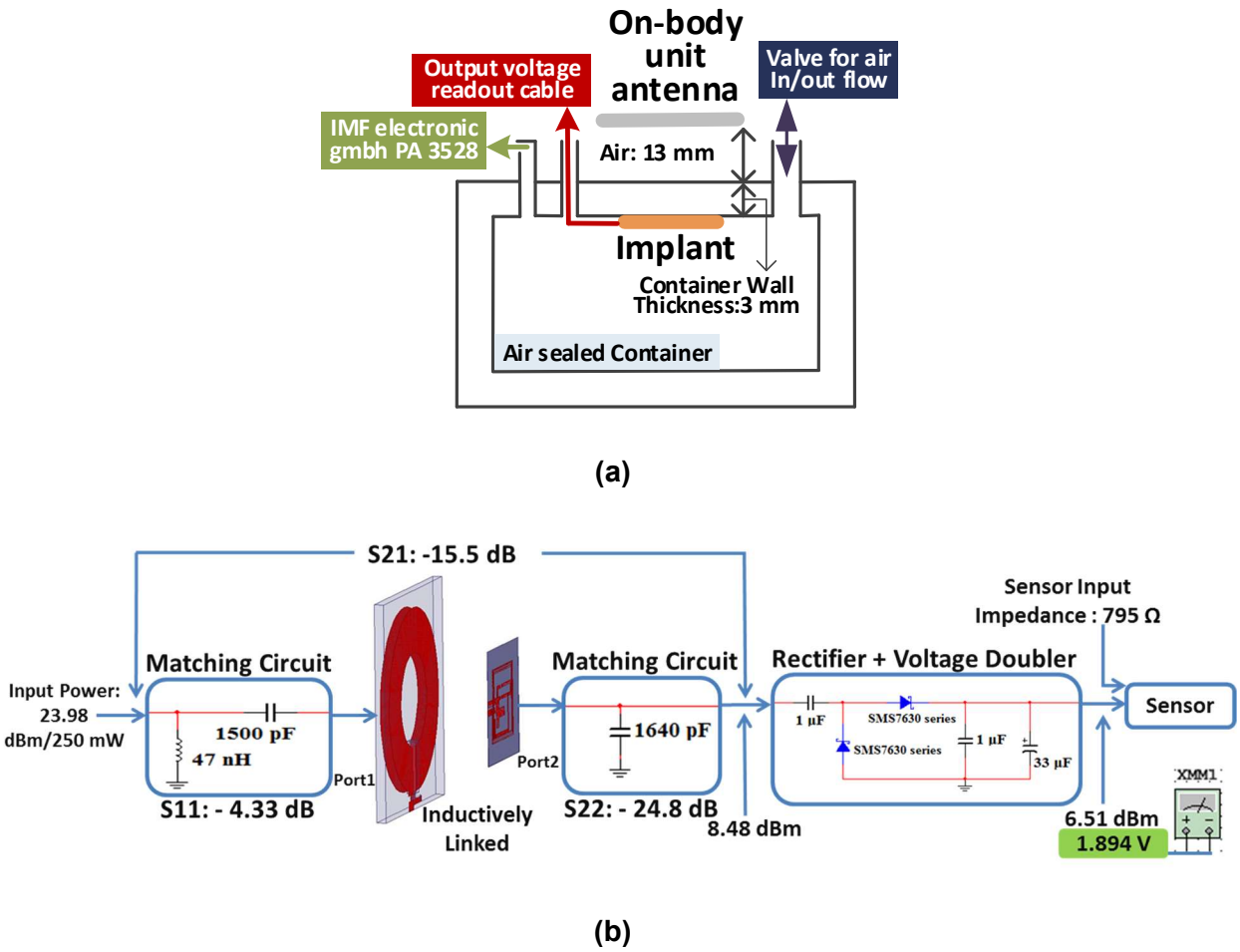

Figure 12. (a) Measurement setup (b) the measured power flow of the developed system in the air without a data transmission unit. [Publication II]

The required power to activate the pressure sensor $(250\,mW)$ is much less than the simulated $P_{t,max} = 1391mW$ at $11\,MHz$ [Publication II]. However, with the addition of the data transmission unit in the implant, we will approach the maximum limit of $P_{t,max}$.

Figure 13 shows the monitored output voltage of the pressure sensor (blue box) with change in the pressure. It is important to note that the system provides relative measurement not the absolute measurement. This means that each value of the output voltage of the sensor does not represent the corresponding pressure value. Instead, it tells us about the relative change in the output voltage of the sensor to an equal change in the pressure. Therefore, it is important to verify the performance of the developed system with the performance when the sensor is powered directly through wire. Figure 13 also shows the output voltage of the same pressure sensor (blue circle) when it is powered through wire with an equal voltage $(1.894\,V)$ as of in the wireless case. Both responses from the same sensor are different, indicating that the wireless power link is not working as expected. The problem is with the measurement setup. For stable reading from the piezoresistive pressure sensor, the input voltage of the sensor should be stable. If voltage at the input of the sensor changes then it

would change the output voltage even without the change in the pressure. To verify this problem, voltage at the input terminals of the pressure sensor is also measured and shown as green line in Figure 13. As can be seen, voltage at the input terminals of the sensor is not constant. Change in the voltage happens due to the expansion of the plastic box as we apply high pressure. As a result, this changes the distance between the coupled antennas. Thus, voltage at the input terminals of the sensor changes. Although a charge storage capacitor of $33\ \mu F$ is added in the implant, but it is unable to stabilize the voltage. This indicates that for voltage stability, a bigger charge storage capacitor and a zener diode as voltage regulator are required. After removing the effect of the voltage change at the input terminals of the sensor as explained in [Publication II], the wirelessly powered pressure sensor has the same response as of the wired powered (see Figure 13).

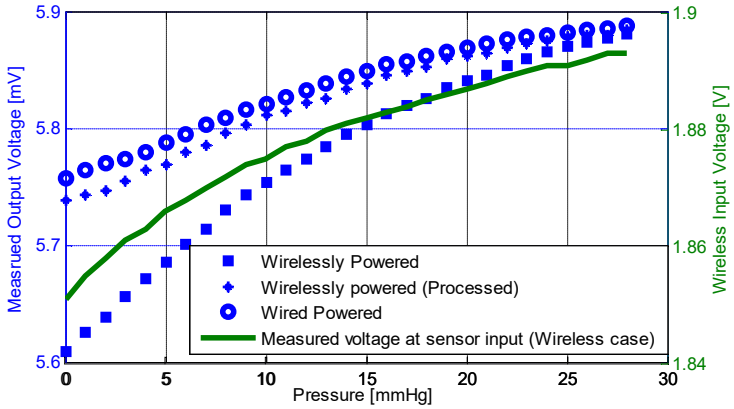

Figure 13. Measured voltage at the sensor output with pressure change and the voltage at the input terminals of the pressure sensor when the antenna of the on-body unit is fed with 250 mW [Publication II].

3.3 Pressure readout experiment in the liquid (water)

The response of the system is also observed in the liquid. In the previous section, the sensor is placed in the air. However, in this section we will discuss the response of the system when the piezoresistive pressure sensor is placed in the liquid. From now onward, we have used Amphenol NPP301A-200A piezoresistive pressure sensor instead of the one that we have used in the previous section due to two reasons. First, due to the small size of the previous sensor, it was difficult to attach to the board. Second, previous sensor has low input resistance ($796\ \Omega$) compared to Amphenol NPP301A-200A ($5000\ \Omega$). This puts requirement to transmit more power to achieve the same voltage at the input terminals of the sensor.

Following changes/improvements in the sensor/measurement setup have been made compared to the previous section [Publication III]:

(i) An addition of zener diode for the stability of the voltage at around $2\ \mathrm{V}$.

(ii) In the measurement, a pig skin of $6\ mm$ thickness is added between the coupled antennas for better modelling of the inductive near-field link compared to the air model in the previous section.

(iii) Only the pressure sensor is exposed to the liquid (water).

(iv) The sensor is coated with $2\mu m$ Parylene C for its normal operation inside the liquid.

Figure 14 (a) shows the measured power flow and S-parameters of the inductive near-field link. With an input power of $19.5\ dBm$ (in previous section $23.98\ dBm$), we are able to achieve $2.122\ V$ (in previous section $1.894\ V$) at the input terminals of the pressure sensor. This happens because of the high input resistance of the pressure sensor as explained in Section 2.2.2. Figure 14 (b) shows the measurement setup. The pressure inside the water column is controlled by water level.

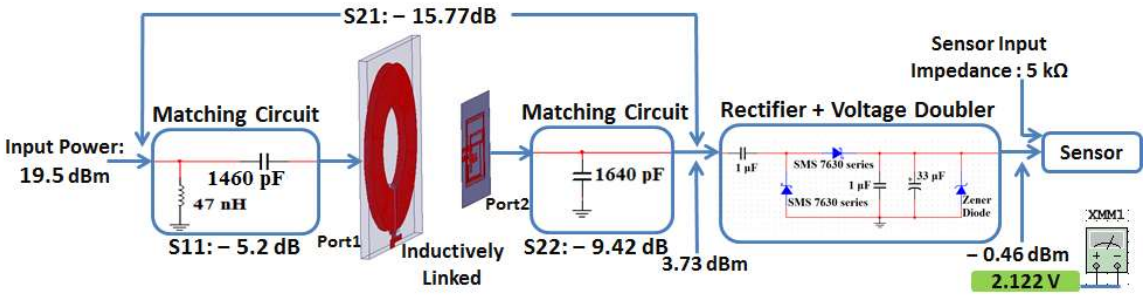

(a)

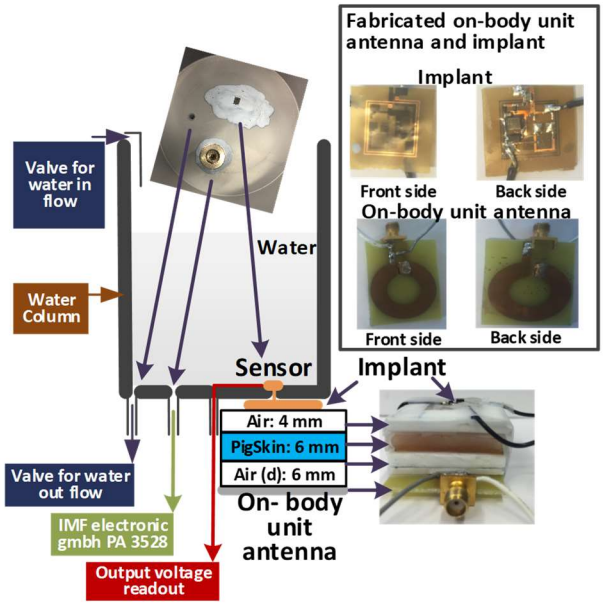

(b)

Figure 14. (a) Measured power flow and S-parameter (b) measurement setup to verify the performance of the developed system in the liquid (water) [Publication III].

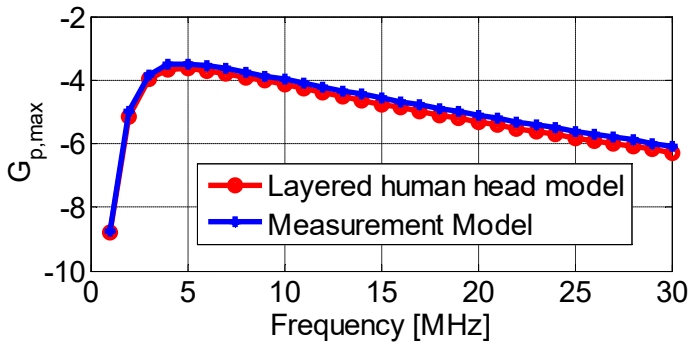

Figure 15. Simulated $G_{p,max}$ for the tissue-layer and the measurement model (Figure 14(b))

Moreover, Figure 15 shows the simulated $G_{p,max}$ for the tissue-layer model and the measurement model. It is clear that adding pig skin of $6\ mm$ thickness between the coupled antennas significantly improve the accuracy of the measurement model compared to the air measurement model of the previous section (Figure 11).

Rectifier efficiency with respect to the change in the input power and the load impedance variation is an important parameter to study for a wireless power transfer system. In our system, load is constant and is known that is why we study the rectifier efficiency with only different input powers. Figure 16 shows the measured rectifier efficiency and the voltage at the input of the sensor with respect to different fed power at the rectifier input. The gap between the coupled antennas and the load impedance are kept the same. The input power to the antenna of the on-body unit is varied from $13.5\ dBm$ to $23.5\ dBm$ with step size of $1\ dB$ by feeding sine wave signal at 11 MHz. This results in power variation from $-2.27\ dBm$ to $7.73\ dBm$ (input power to the antenna of the on-body unit – $15.77\ dB$) at the rectifier input terminals. The rectifier efficiency increases linearly with the increase in the feed power until $5.5\ dBm$. However, after $5.5\ dBm$ input power, the increase in rectifier efficiency is not linear any more.

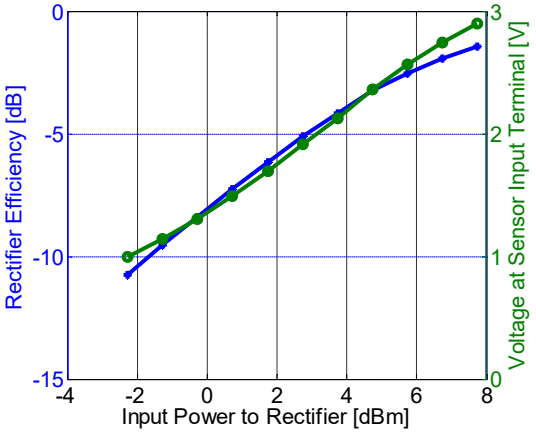

Figure 16. Measured rectifier efficiency and the voltage at the input of the sensor with the change in the transmission power

Figure 17 shows the measured voltage at the output of the sensor with the change in the pressure. The pressure is changed in both Up/Down directions with a step size of $1\ mmHg$. This verifies the system response in both directions. Moreover, two sets of Up/Down measurements are performed to verify the repeatability of the system. We can conclude as following:

(i) The sensor's response is linear over the studied pressure range. A total of $773\ \mu V$ change in the voltage from $18.617\ mV$ to $19.390\ mV$ is observed corresponding to $30\ mmHg$ pressure change from $0\ mmHg$ to $30\ mmHg$.

(ii) The sensor shows an average hysteresis of only $13\ \mu V$ between the increasing and the decreasing pressure.

Even with hysteresis, there is clear distinction between the voltages corresponding to the adjacent pressure values. This attests $1\ mmHg$ resolution in the pressure readout.

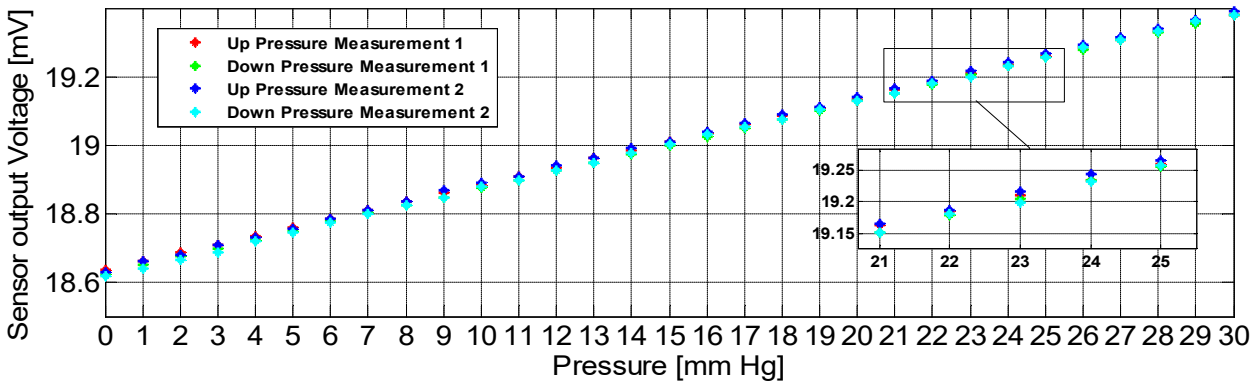

Figure 17. Measured output voltage of the sensor with the change in the pressure in liquid (water).

The results indicate that the presented ICP monitoring system without a data transmission unit showed an excellent response. However, we have simplified many things in the simulation and in the measurement. For example, in the simulation, there is no coating material around the implant. Although, in the measurement, we have used pig skin of $6\ mm$ thickness between the coupled antennas for inductive near-field link, however, in real application, the sensor is supposed to place in the CSF. The next chapter discusses the data transmission unit, the addition of the coating material in the simulation and presents the results from experiments carried out in a setting which mimics the biological operation environment.

4 Intracranial pressure monitoring system with a data transmission unit

This chapter presents the simulation and measurement results from an ICP monitoring system with a data transmission unit. Figure 18 shows the detailed description of the ICP monitoring system with a data transmission unit. The on-body unit powers the implant and consists of a powering module, loop antenna and a matching network for the loop antenna. The implant has a 2-turns coil antenna that is inductively coupled with the antenna of the on-body unit. A matching network is used for matching the 2-turns coil antenna. A rectifier consists of schottky diodes and capacitors for RF-to-DC conversion and voltage doubling, Zener diode as voltage regulator and super capacitor for charge storage. A piezoresistive pressure sensor monitors the pressure. A differential amplifier amplifies the difference in the output voltage of the pressure sensor and drives the VCO at ISM band of $2.45\ GHz$. Both amplifier and VCO are powered through rectifier as shown in the Figure 18. The output of the VCO is connected to the far-field antenna. The output of the piezoresistive pressure sensor is sensitive towards the change in the pressure. This means that differential output of the pressure sensor changes with the change in the pressure. Therefore, we are converting the voltage change of the sensor to the frequency change of the VCO output signal. By monitoring the change in the frequency of the transmitted signal from the implant, we can monitor the change in pressure. The signal transmitted from the implant is received by the off-body unit placed at $1\ m$ from the implant. The off-body unit has $\lambda/2$ dipole antenna that is connected to the spectrum analyzer (SA).

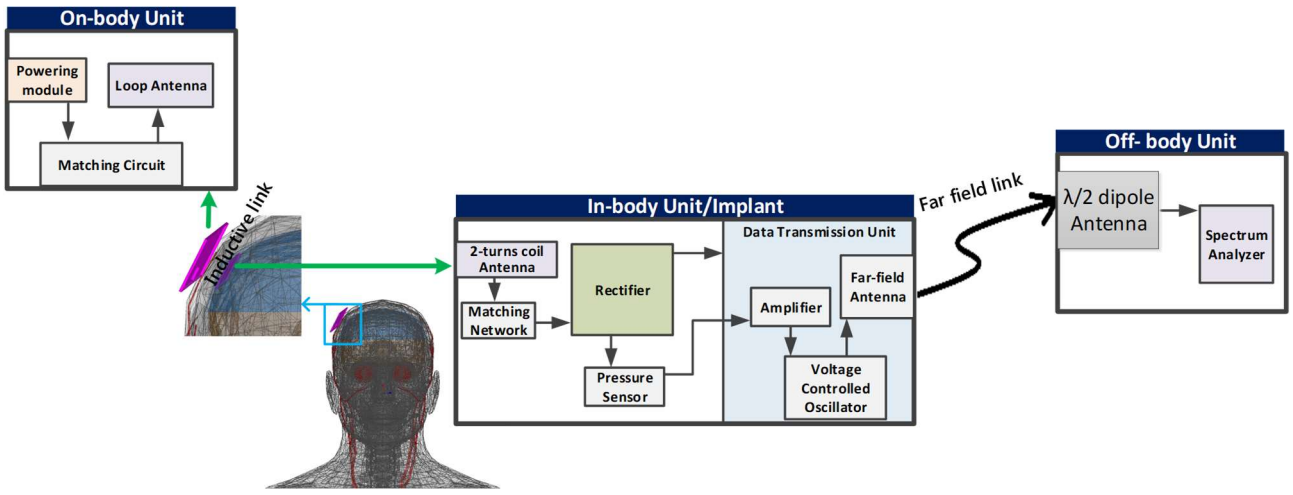

Figure 18. The detailed description of the wirelessly powered ICP monitoring system with a data transmission unit.

In this chapter, we present the simulation and measurement results of the far-field antenna, the effect of the coating on the inductive near-field link and on the gain of the far-field antenna. In addition, present a comparison of tissue-layer and anatomical human head model provided by HFSS v15 and

finally, complete implant design and measurement results in a setting mimicking the human head environment.

4.1 Far-field antenna simulation and measurement

Based on the far-field implant antenna design considerations explained in Section 2.3, we selected a co-planar spiral antenna structure. The spiral structure is selected over meander because spiral provides lower resonance frequency and higher radiation efficiency. The radiation efficiency of meander structure is low because of the opposing current direction in the adjust arms of the radiating patch [27-28]. Figure 19 shows the top view of the simulated far-field antenna structure [Publication IV]. Tissue-layer model explained in previous chapter (Figure 10(c)) is used for the simulation. The implant is coated with commercially available silicone with a total thickness of $1\ mm$ [Publication IV]. The antenna dimensions "Tf", "Sf" and "W" are fixed due to the size of the VCO, however, the rest of the dimensions are optimized to achieve the resonance at $2.45\ GHz$ with maximum size limits "$L + Lg + Sf = 6\ mm$" and "$Wg + Ws = 5\ mm$". The maximum limits are imposed due to available size on the implant. The far-field antenna is designed on the flexible polyimide substrate as explained in the previous section. At first step, the antenna is simulated as individual. The material close to the antenna disturbs the current flow in the antenna and affects the antenna resonance frequency and radiation pattern. Therefore, after simulating the antenna individually, we placed the antenna on the implant surrounded by the 2-turns coil antenna and other copper traces for electronics components. This requires retuning of the antenna dimensions to bring the resonance frequency back to $2.45\ GHz$. Figure 20 shows the layout of the implant front and back sides. Table 1 shows the final far-field antenna dimensions.

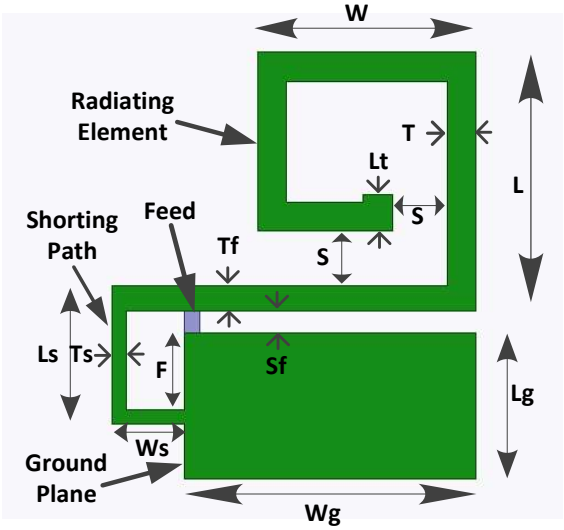

Figure 19. Top view of the far-field antenna structure [Publication IV].

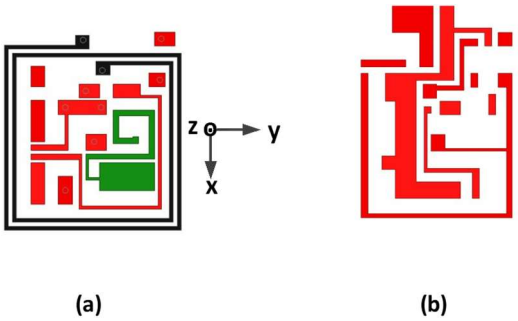

Figure 20. (a) The front side of the implant (red traces represent electronic circuitry, black represents 2-turns coil antenna and green represents the implant antenna) (b) the backside of the implant (red traces for electronic circuitry) [Publication IV].

Table 1. Optimized dimensions of the far-field antenna presented in Figure 19 [Publication IV].

Symbol	L	W	Lg	Wg	Ls	Ws	T	S	Lt	Sf	Tf	F	Ts
Value [mm]	3.55	3	2	4	1.9	1	0.4	0.75	0.5	0.3	0.35	1.05	0.2

4.1.1 Simulation results of the far-field antenna

Figure 21 shows the simulated reflection coefficient of the far-field antenna. The antenna has $-10\ dB$ bandwidth of $280\ MHz$. Figure 22 shows the E-field distribution of the antenna at $2.45\ GHz$. Antenna is acting as a $\lambda/2$ resonator at $2.45\ GHz$ (see Figure 22). Moreover, Figure 23 and 24 show the antenna 3-D and 2-D gain patterns. It is important that the antenna should not radiate towards the brain to avoid any harm due to the radiation. From Figure 23, it is clear that the far-field antenna main beam is directed away from the brain. Moreover, antenna has small side and back lobs. The simulated antenna gain, directivity and radiation efficiency are $-19.63\ dB$, $-4.33\ dB$ and $0.5\ \%$ respectively [Publication IV].

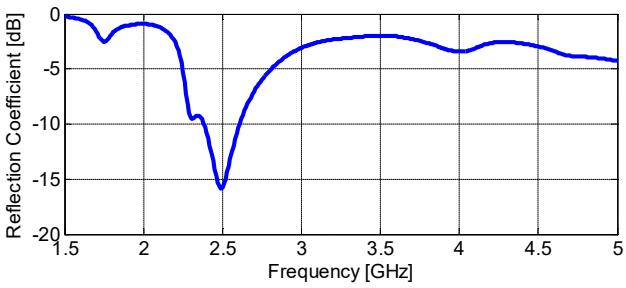

Figure 21. The simulated reflection coefficient in dB [Publication IV].

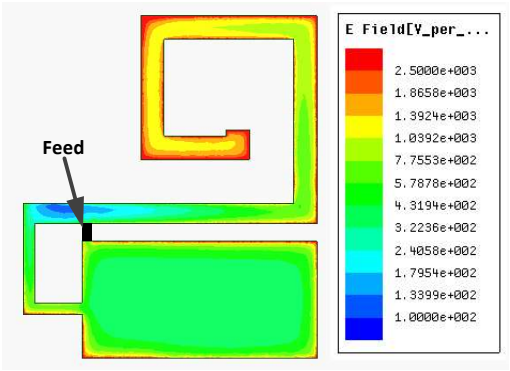

Figure 22. E-field (V/m) distribution at the far-field antenna surface at 2.45 GHz [Publication IV].

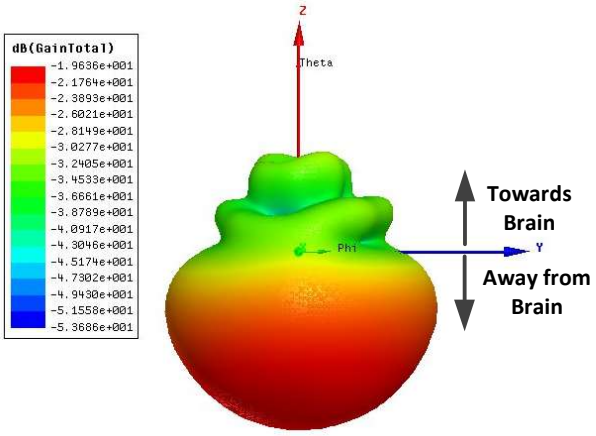

Figure 23. 3-D gain pattern of the far-field antenna at 2.45 GHz [Publication IV].

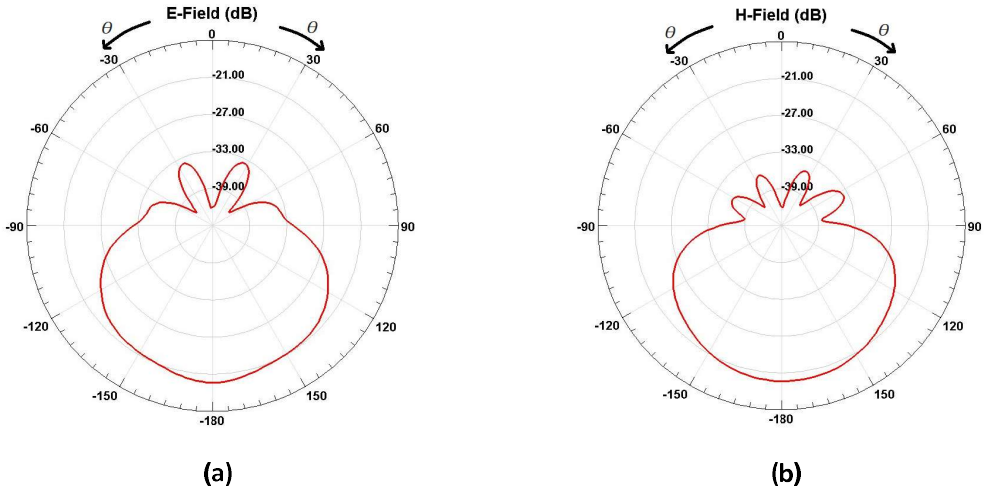

Figure 24. Far-field antenna 2-D gain pattern at 2.45 GHz (a) E-plane (b) H-plane [Publication IV].

Although the gain of the antenna and the radiation efficiency are low. Still, it radiates electromagnetic energy. Therefore, it makes important to check either antenna full fills the SAR limit or not. In the simulation model, although the antenna is facing away from the brain but closest tissue layers to the antenna are the bone and the brain. Therefore, we estimate the SAR in both tissue layers as explained in [Publication IV]. The maximum output power of the VCO is $0.5\ mW$. Therefore, we estimate the SAR_{max} for $0.5\ mW$ input power. Table 2 shows the simulated $P_{t,max}$ and SAR_{max} for both tissue layers [Publication IV]. From Table 2, it is clear that bone tissue layer has the highest SAR_{max} and puts the limit to $P_{t,max}$ from the far-field antenna. This makes sense because the antenna radiates towards the bone and small amount of electromagnetic energy goes towards the brain. Another important point to note is that $P_{t,max}$ for the bone is much higher than $0.5\ mW$ [Publication IV]. As SAR_{max} generated in the bone layer limits the $P_{t,max}$, therefore, we have plotted the local SAR distribution at the bone interface when far-field antenna is fed with $0.5\ mW$ at $2.45\ GHz$ as shown in Figure 25.

Table 2. Simulated $P_{t,max}$ and SAR_{max} for the bone and the brain tissue layers [Publication IV].

Layer	SAR_{max} [W/kg] for 0.5 mW input power	$P_{t,max}$ [mW]
Bone	0.1446	5.53
Brain	0.0104	7.63

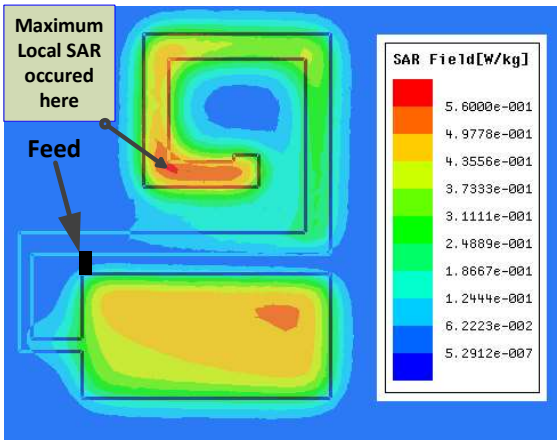

Figure 25. Local SAR (W/kg) distribution at the bone interface when far-field antenna is fed with 0.5 mW at 2.45 GHz [Publication IV].

4.1.2 Measurement results of the far-field antenna

Small antenna with low gain and designed for human head environment are difficult to measure due to the following reasons:

(i) Due to $0.4\ mm$ gap between the ground and the radiating patch, it is difficult to connect the antenna with a normal SMA connector. Therefore, we have used a micro-coaxial cable for this connection. Also connecting the micro-coaxial cable requires great care.

(ii) Due to the small size of the antenna, even the small size of the micro-coaxial can influence the measurement results. Therefore, we used the port extension feature in the vector network analyser (VNA) to remove the micro-coaxial cable impact from the measurement.

(iii) The far-field antenna is designed for human head environment; therefore, it is important to measure the antenna performance in an environment close to the human head. For this purpose, we developed a liquid phantom by adding salt and sugar into the water as explain in [52] that resulted in the dielectric properties close to the human head dielectric properties [Publication IV].

(iv) Due to the low gain and liquid surrounding the antenna, it is not possible to measure the antenna gain through normal near-field or far-field field measurement methods. The reason is that during the measurement the liquid surface is not stable due to movement of the stand on which the antenna is placed. Therefore, we estimate the antenna gain at $2.45\ GHz$ through Friis transmission formula (see Section 2.1) as explained in [Publication IV]. Moreover, the esimated antenna gain is compared with the simulated antenna gain that is simulated in a setting similar to measurement setup.

Figure 26 shows the setup for measuring the reflection coefficient and measured reflection coefficient. Figure 26 (b) also shows the simulated reflection coefficients for tissue-layer and liquid phantom models. It is clear that the liquid phantom model is a good approximation of the tissue-layer model. Moreover, the measured reflection coefficient follows the simulated one. Although the measured $-10\ dB$ bandwidth $(160\ MHz)$ of the antenna is smaller than the simulated, but it covers the ISM band of $2.45\ GHz$.

For gain estimation, the VCO is connected to the far-field antenna and activated through an external DC voltage supply. The fed power from the VCO to the far-field antenna is $-3\ dBm\ (0.5\ mW)$. The transmitted signal at $2.45\ GHz$ from the far-field antenna is received by a $\lambda/2$ dipole antenna whose parameters (gain and reflection coefficient) are known. The distance between the transmitting and the receiving antennas is also known. Therefore, using equation (2.4), we estimated the far-field antenna gain as explained in [Publication IV]. Figure 27 shows the measurement setup and the measurement picture for the far-field antenna gain measurement. To verify the consistency between

the results, the gain of the antenna is estimated at two distances ($0.5\ m$ and $1\ m$) between the transmitting and the receiving antennas. Table 3 shows the estimated gains at two distances. The simulated and measured gains of the far-field antenna are within $3\ dB$ difference [Publication IV].

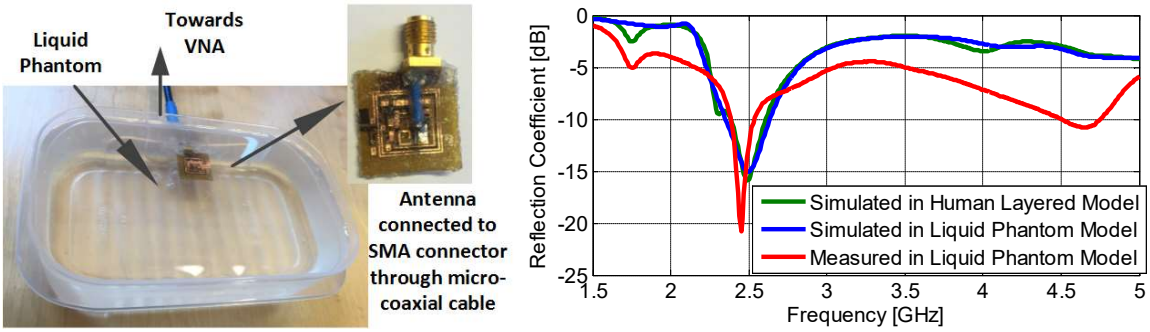

Figure 26. (a) Setup for reflection coefficient measurement (b) measured and simulated (tissue-layer and liquid phantom models) reflection coefficients in dB. [Publication IV]

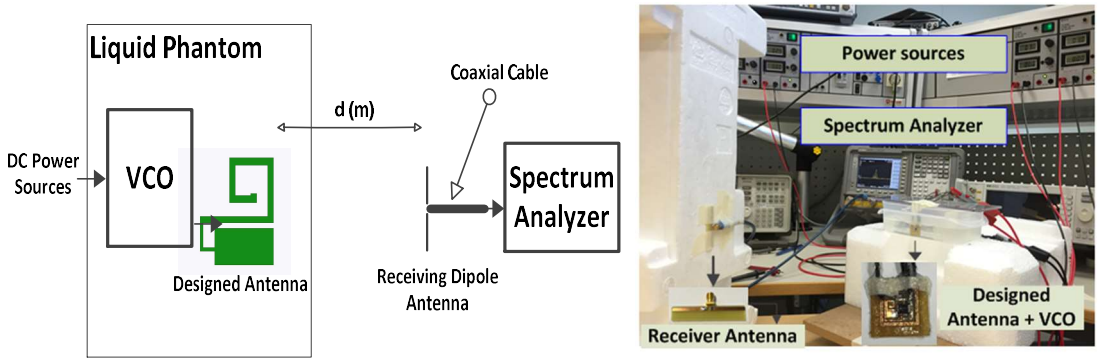

Figure 27. Far-field antenna gain measurement (a) measurement setup (b) measurement picture [Publication IV].

Table 3. Received power level by the $\lambda/2$ dipole antenna and estimated gain of the far-field antenna [Publication IV].

Distance (d) [m]	Received Power Level [dBm]	Estimated Gain [dBi]
0.5	- 53.0	-23.25
1	- 58.6	-22.94

4.2 Inductive link modelling using an anatomical human head model and effect of the coating

The tissue-layer model presented in Figure 10(c) is simple. However, we have also verified the inductive near-field link modelling in an anatomical human head model provided by ANSYS HFSS v15. The anatomical human head model is detailed and complex, therefore takes significantly large time to simulate the inductive near-field link. In an anatomical human head model, the implant is placed in the CSF and the antenna of the on-body unit is placed at $5\ mm$ away from the skin as shown in Figure 28. For biomedical application, the implant should either be made of biocompatible material or coated with biocompatible material. Therefore, in the simulation, the implant is covered with a total of $1\ mm$ thick coating of the biocompatible adhesive silicone (MED-2000.) Although the actual implant after the fabrication is coated with two layers of the coatings. First, it is covered with $1\ mm$ thick silicone and then with $2\ \mu m$ Parylene C. However, in the simulation, we only consider silicone coating because effect of very thin Parylene C coating on the inductive near-field link can be neglected.

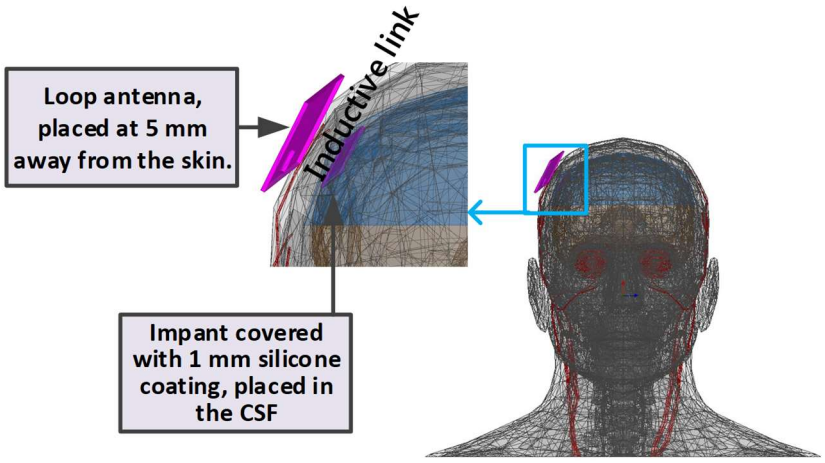

Figure 28. The modelling of the inductive near-field link in an anatomical human head model provided by ANSYS HFSS v15. Implant is placed in the CSF and coated with a total 1 mm thick biocompatible silicone.

Figure 29 presents the $G_{p,max}$ of the inductive near-field link in an anatomical human head model with and without the coating material. We can conclude as following [Publication VI]:

(i) The optimum frequency without the coating for maximum $G_{p,max}$ is $6\ MHz$ which is the same as in the case of the tissue-layer model (Figure 10 (c)). This means that both models have the same response in terms of optimum frequency when there is no coating. However, $G_{p,max}$ is $-8.6\ dB$ in the anatomical model compared to $-3.0\ dB$ in the tissue-layer model. CSF is lossy material and placing the implant in the CSF adds more loss to the inductive near-field link.

(ii) Adding the coating material, improves the $G_{p,max}$ and shifts the optimum frequency from $6\ MHz$ to $15\ MHz$. At $15\ MHz$, there is an improvement of $6\ dB$ in $G_{p,max}$ with coating material.

(iii) Therefore, coating not only provides biocompatibility of the implant but also improves the inductive near-field link efficiency. Based on new simulation results, from now onward, we have shifted the optimum frequency to $15\ MHz$ for the inductive near-field link.

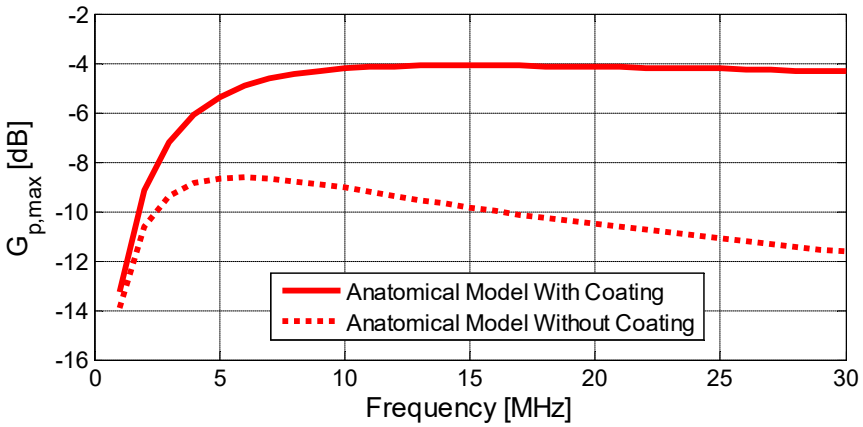

Figure 29. Simulated $G_{p,max}$ in an anatomical human head model with and without the coating [Publication VI].

Moreover, coating has significant impact on the gain of the far-field antenna. Figure 30 shows the far-field antenna gain by varying the coating thickness. For very thin coating, the gain of the antenna is low because the distance between the lossy human tissues and the antenna radiating patch is small. As the coating thickness increases, gain gets stable.

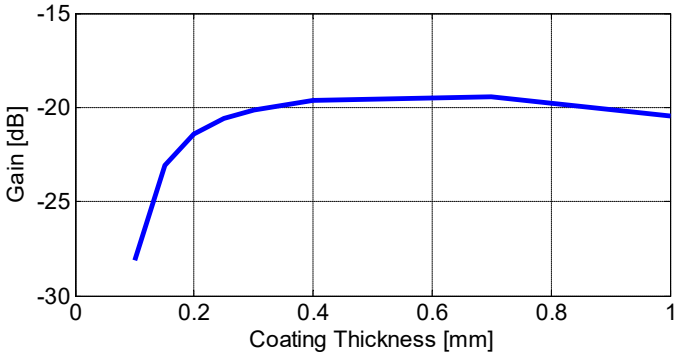

Figure 30. The impact of coating thickness on the far-field antenna gain [dB] [Publication IV].

4.3 Pressure readout experiment in a setting mimicking the dielectric properties of the human head

From the previous section, it is concluded that optimum inductive near-field link operation frequency is $15\ MHz$. Moreover, at $15\ MHz$ the $P_{t,max}$ is $940\ mW$ (see Figure 11). Therefore, we have tuned the matching networks for both 2-turns loop antenna (on-body unit) and 2-turns coil antenna (implant) at $15\ MHz$. Apart from this, the data transmission unit (amplifier, VCO and far-field antenna) is also added in the implant. Figure 31 shows the final implant layout on the thin and flexible polyimide substrate.

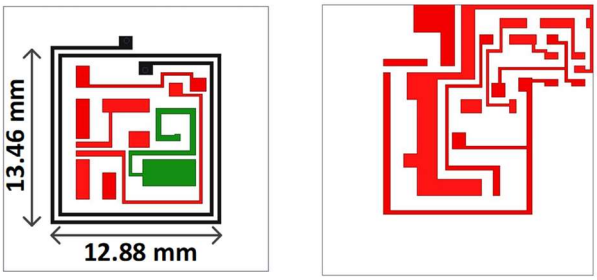

Figure 31. (a) The front side of the implant (a 2-turns coil antenna, a far-field antenna and traces for other components) (b) the backside of the implant (traces for components attachment) [Publication V].

The VCO need around $3\ V$ for activation, therefore, we have added a super capacitor of $11\ mF$ (CPH3225A) instead of $33\ \mu F$ capacitor. Moreover, a Zener diode is used as a voltage regulator to stable the voltage around $3\ V$. After designing, the implant is fabricated and coated first with $1\ mm$ thick biocompatible silicone and then $2\ \mu m$ Parylene C.

4.3.1 Measurement setup

For an inductive near-field link, the material between the coupled antennas is important and for the far-field link, the surrounding environment of the implant should have similar dielectric properties to the human head. As explained in Section 3.3, pig skin of $6\ mm$ thickness provides good approximation. Therefore, for the inductive link, we used the same setting as explained in Section 3.3.

However, for the far-field link, as explained in Section 4.1, we developed a liquid by adding salt and sugar that mimics the human head dielectric properties. We used the same liquid. The implant is placed in a glass bottle and glass bottle is filled with that liquid. The pressure inside the glass bottle is controlled by pressure controlling device ADT761. Moreover, we have increased the temperature of the liquid inside the glass bottle through heating plate. The temperature of the liquid is maintained at $37°C$ (body temperature) during the measurement.

The 2-turns loop antenna is placed outside the glass bottle and is connected to the signal generator. The total distance between the implant and the 2-turns loop antenna is $16\ mm$. A $\lambda/2$ dipole antenna of off-body unit is placed at $1\ m$ distance from the glass bottle and is connected to the spectrum analyzer. Figure 32 shows the measurement setup for monitoring the pressure in a setting mimicking the human head dielectric properties. Figure 33 shows the power flow of the developed ICP monitoring system and measured S-parameters of the inductive near-field link. It is important to note that on-body unit antenna is fed with $31\ dBm$ $(1259\ mW)$, however, $P_{t,max}$ at $15\ MHz$ is $940\ mW$. The reflection coefficient of the on-body unit antenna is $-5.3\ dB$, which means that only $889\ mW$ is coupled to the implant antenna and rest is reflected back. The reflection coefficient of the on-body unit antenna is high because small loop antennas at lower frequency are difficult to match to $50\ \Omega$ due to small real part of their input impedances. As the antenna of the on-body unit is fed with $31\ dBm$, this activates the implant and implant starts monitoring the pressure. With the change of the pressure inside the glass bottle, the frequency of the transmitted signal from the implant at ISM band changes. Therefore, by monitoring the change in the frequency of the implant signal, we can estimate the variation in the pressure.

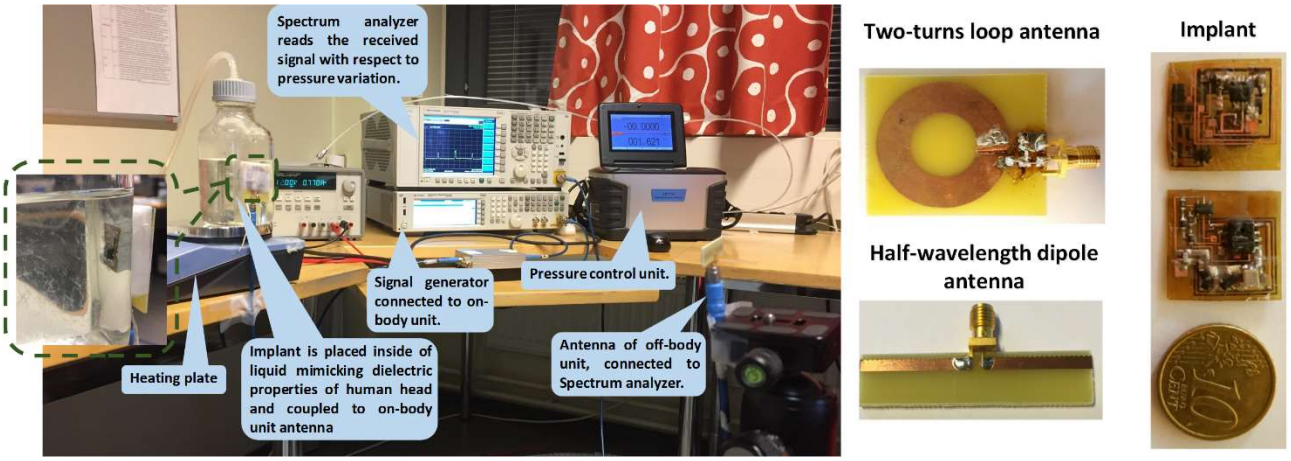

Figure 32. Measurement setup for monitoring the pressure in a setting mimicking the dielectric properties of the human head and fabricated implant, on- and off-body unit antennas [Publication V].

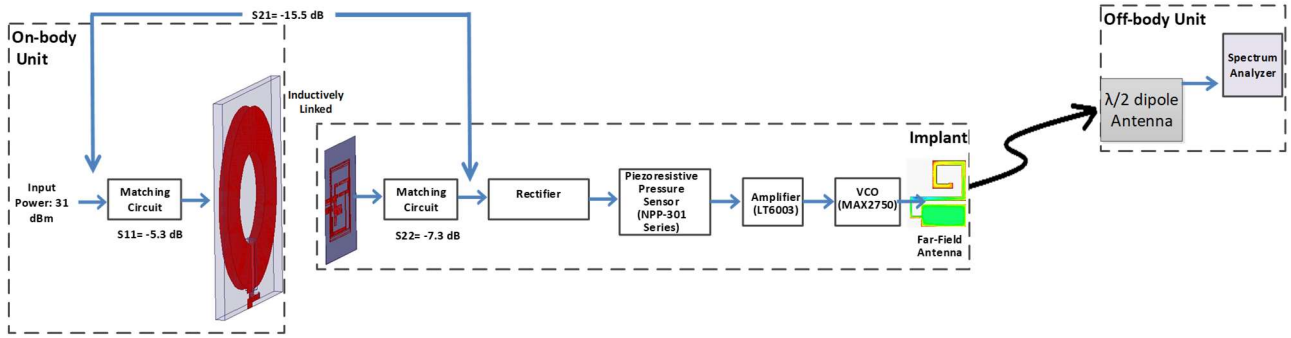

Figure 33. Power flow and measured S-parameter of the ICP monitoring system [Publication V].

4.3.2 Pressure readout measurement results

The pressure measurement follows the same steps as in Section 3.3. The pressure inside the glass bottle is varied from $-\ 3\ mmHg$ to $33\ mmHg$ with a step size of $3\ mmHg$ in both Up and Down directions. Two sets of pressure measurements are performed to verify the repeatability of the developed ICP monitoring system. Figure 34 shows the change in the frequency of the received signal from the implant with the change in the pressure. A total of $5.2\ MHz$ change in the frequency is observed with $36\ mmHg$ change in the pressure. This corresponds to $145\ kHz$ change per $1\ mmHg$. However, an average hysteresis is $150\ kHz$. This means that system shows a resolution of $2\ mmHg$. The resolution of the system without the data transmission unit was $1\ mmHg$. Therefore, with the addition of the data transmission unit the resolution of the system decreased to $2\ mmHg$.

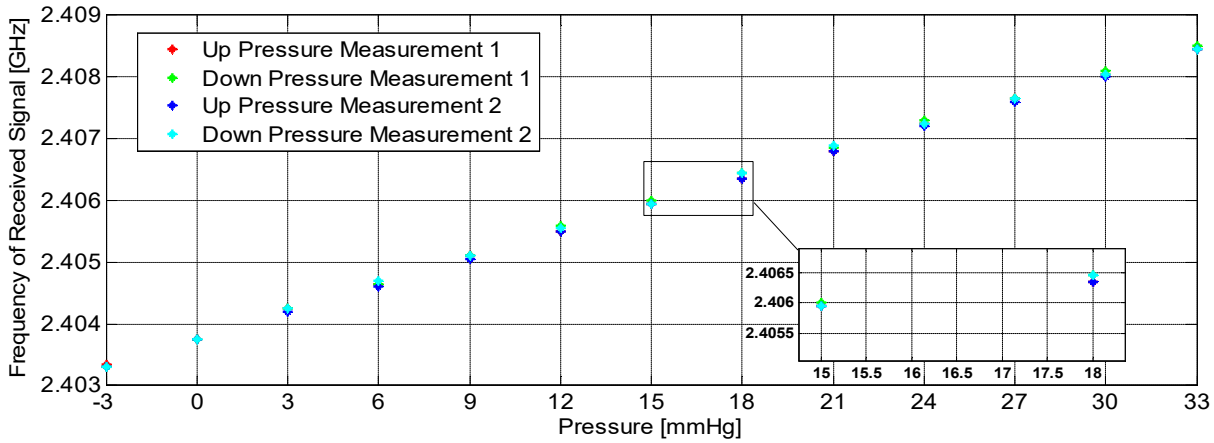

Figure 34. Measured frequency of the received signal from the implant with the change in the pressure [Publication V].

In real application, the implant is fixed; however, the on-body unit antenna can be misaligned, for example, due to patient movement. Therefore, it is important to verify the response of the ICP monitoring system if small misalignment of the order of $2\ mm$ is occurred. Figure 35 shows the error in pressure readout if the antenna of the on-body unit is misaligned. In this measurement only coupled antennas are misaligned on X- and Y- axis (lateral misalignment) on a rectangular coordinate axis. However, separation between them and fed power to the antenna of the on-body unit are kept constant [Publication V]. The error in the pressure readout is estimated based on the shift in the frequency of the received signal as explained in [Publication V]. The error in the pressure readout is significantly large for small misalignment. This happens due to the structure and the size of the antenna of the on-body unit. The 2-turns loop antenna of the on-body unit has strong H-field in the middle of the antenna, however, the H-field decays sharply when moving away from the centre [Publication V].

Although the developed ICP monitoring system with a data transmission unit showed an excellent performance for monitoring the change in the pressure. However, small misalignment significantly

affects the performance of the system. From Figure 35, the error in the pressure readout due to misalignment is always negative. Negative means that the system shows lower pressure value compare to the actual due to misalignment effect. One solution to the problem is to move the antenna of the on-body unit and search for the maximum pressure value [Publication V]. Next chapter discusses about the solution to overcome the impact of small misalignment on the performance of the system by proposing a 3-D antenna structure for the on-body unit.

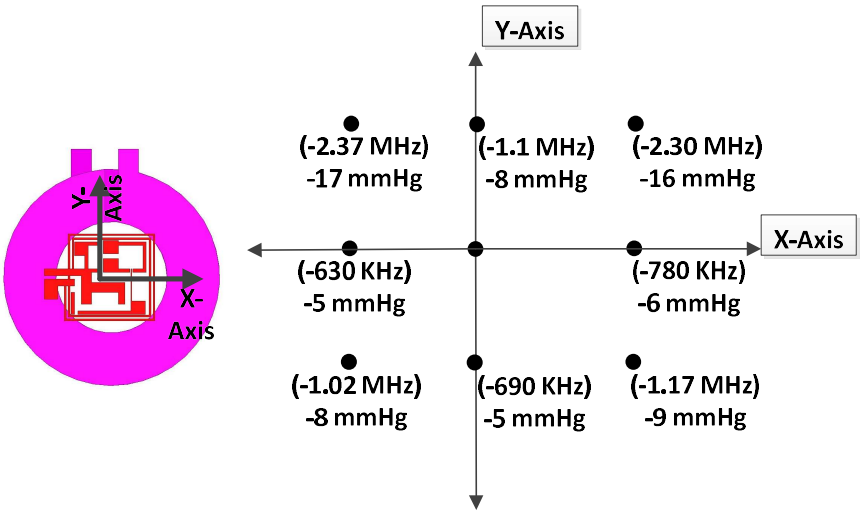

Figure 35. Measured shift in the frequency of the received signal and estimated error in the pressure readout due to small misalignment between the coupled antennas [Publication V].

5 Effect of misalignment between inductively coupled antennas and temperature on the response of the intracranial pressure monitoring system

As discuss in the previous chapter, small lateral misalignment significantly affects the performance of the developed ICP monitoring system. In this chapter, we explain that 3-D loop antenna helps to overcome the impact of small lateral misalignment between the inductively coupled antennas. Moreover, we also present the impact of temperature change on the response of the developed ICP monitoring system.

5.1 3-D antenna for an on-body unit

As explained in the previous chapter, the H-field of the 2-turns loop antenna of the on-body unit decays sharply as we move away from the center of the antenna. In our system, both antennas of the on-body unit and the implant are tightly coupled. Moreover, the size of both antennas are relative the same. This means that small misalignment between the inductively coupled antennas leads to a significant variation in the magnetic flux passing through the 2-turns coil antenna of the implant, as explained in Section 2.2.2. Therefore, the voltage at the implant terminals drops. This resulted in the shift of the frequency of the received signal to lower value even at the same pressure value.

Several studies [53-58] have been reported by many researchers that present semi-analytical or analytical solutions for the analysis of misaligned coils. They present analysis either for lateral or both lateral and angular misalignments. As explained in Section 2.2.2, an inductively coupled system where the antenna of the on-body unit has bigger diameter compared to the implant antenna is more robust towards the misalignment between the inductively coupled antennas. However, the antenna of the on-body unit with bigger diameter has higher SAR due to stronger E-field peaks on the skin surface and $G_{p,max}$ can be lower for the system [Publication VIII]. Moreover, our goal is to keep the on-body unit simple, low cost, small and lightweight.

A 3-D antenna presented in [Publication VIII] can significantly reduce the error in the pressure readout due to misalignment between the inductively coupled antennas. The 3-D antenna has bigger diameter with the same $G_{p,max}$ and $P_{t,max}$ as of the 2-turns loop antenna. Figure 36 shows the initial and the final design of the 3-D loop antenna. Detailed optimization steps for 3-D loop antenna are explained in [Publication VIII]. However, here we can summarize these steps as following:

(i) First, 3-D loop antenna length (D) and height (H) are optimized for maximum $G_{p,max}$.

(ii) Second, cut angle (A_C) and cut height (H_C) are optimized for the same $P_{t,max}$ and $G_{p,max}$ as of the 2-turns loop antenna.

To get customized antenna structure, we use polylactic acid (PLA) with a thickness (S_T) of 3 mm as a substrate. The substrate is printed through 3-D printer as explained in [Publication VIII].

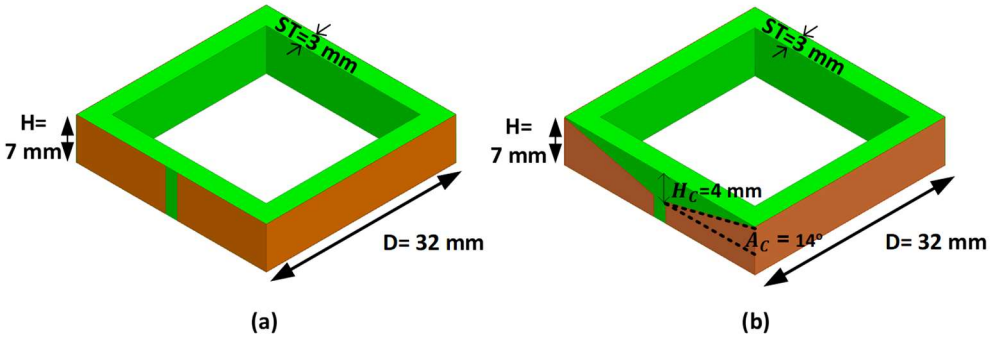

Figure 36. 3-D loop antenna (a) initial design (b) final design [Publication VIII].

The optimization of cut angle (A_C) and cut height (H_C) significantly reduces the E-field peaks at the surface of the skin. Figure 37 shows the E-field and local SAR distributions at the surface of the skin. Moreover, Figure 38 shows the vector H-field plot of the final 3-D loop antenna. It is clear the H-field is uniform within the diameter of the 3-D loop antenna.

A comparison of normalized H-field distribution between the 3-D loop antenna and the 2-turns loop antenna is shown in Figure 39. The H-field is extracted on the plane parallel to the antenna and at $16\ mm$ distance. It is clear from Figure 39 that H-field of the 3-D loop antenna decays relatively slowly compare to the 2-turns loop antenna as we move away from the centre of the loop antennas.

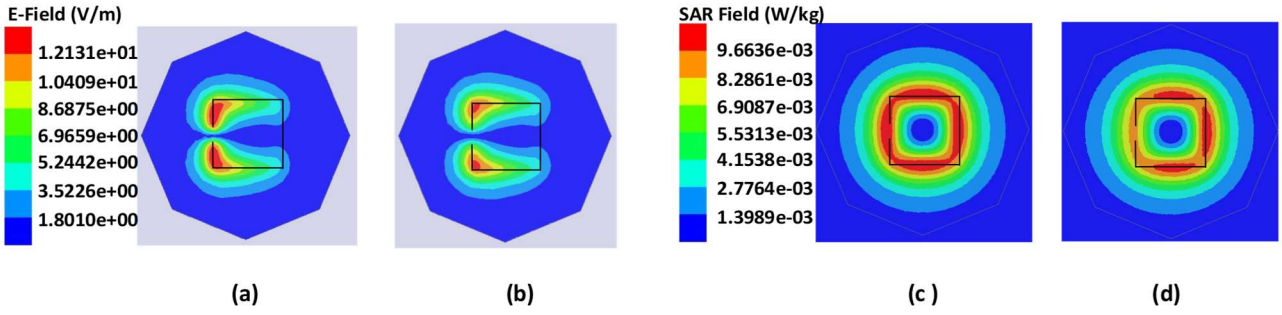

Figure 37. E-field (V/m) distribution of (a) initial (b) final 3-D loop antenna at the surface of the skin. Local SAR (W/kg) distribution of (c) initial (d) final 3-D loop antenna at the surface of the skin. Frequency for distributions is 15 MHz. [Publication VIII]

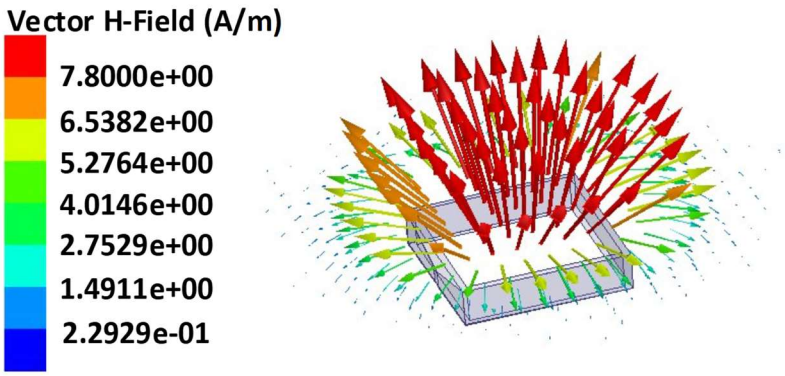

Figure 38. Vector H-field distribution (A/m) plot of final 3D loop antenna on the surface of the skin at 15 MHz [Publication VIII].

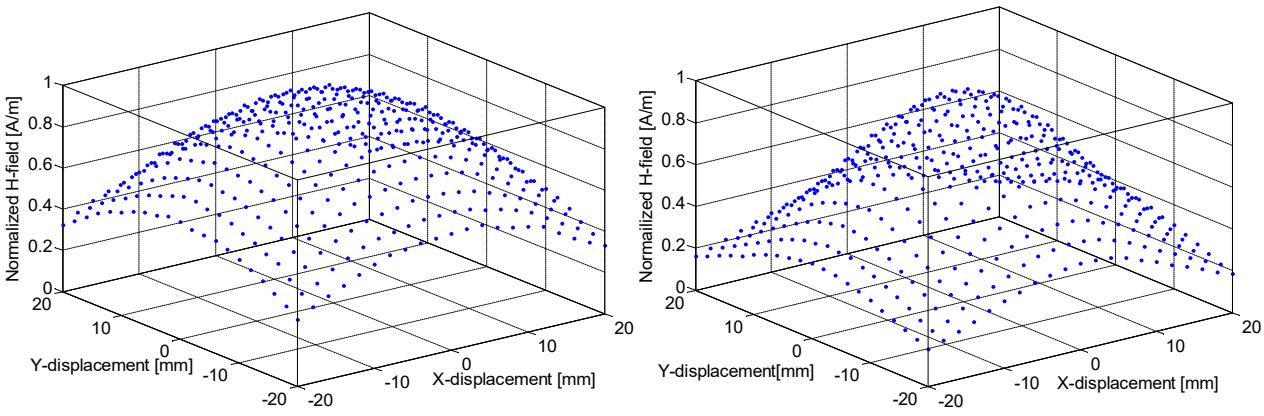

(a) (b)

Figure 39. Normalized H-field distribution extracted at 16 mm away from the antenna in a plane parallel to (a) 3-D loop antenna (b) 2-turns loop antenna [Publication VIII].

5.1.1 Pressure readout and misalignment measurements using a 3-D loop antenna

After the antenna fabrication, first, pressure readout measurement is done using a 3-D loop antenna and then the misalignment measurement. The measurement setup explained in Section 4.3.1 is used for pressure readout measurement. Similarly, the misalignment measurement is done by following the same procedure explained in Section 4.3.2. Figure 40 shows the pressure readout measurement. The system has a similar response with the 3-D loop antenna compared to the 2-turns loop antenna (Figure 34). Moreover, results from the misalignment measurement are shown in Figure 41. For comparison, pressure readout error due to misalignment for a 2-turns loop antenna is also shown. The measurement results indicate that there is significant reduction in the pressure readout error with 3-D loop antenna. Although, error is not completely remove, however, the improvement is significant.

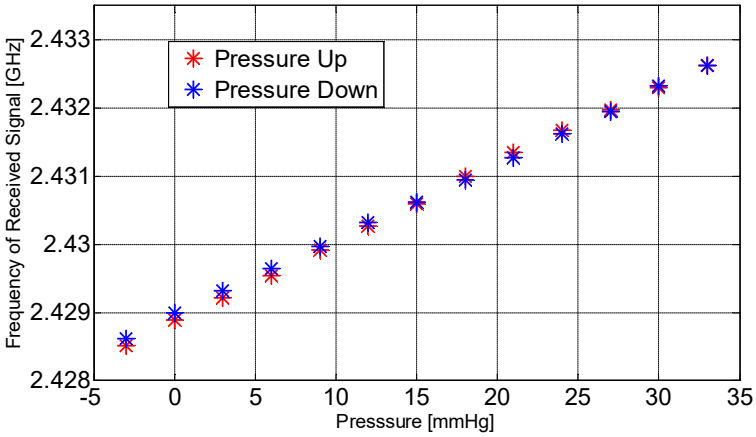

Figure 40. Frequency of the received signal with variation in the pressure using a 3-D loop antenna [Publication VIII].

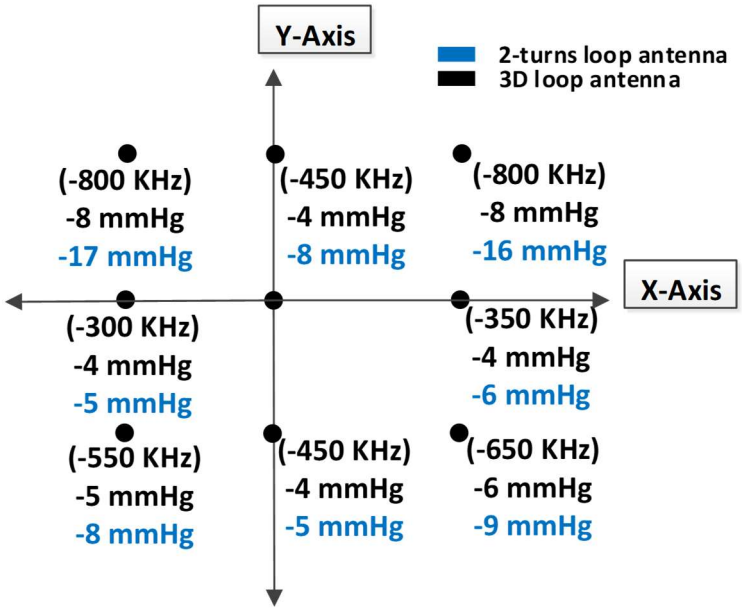

Figure 41. Shift in the frequency of the received signal due to misalignment between the coupled antennas. Pressure readout error of 3-D loop antenna. Also pressure readout error of 2-turns loop antenna. [Publication VIII]

5.2 Effect of temperature on the performance of the ICP monitoring system

In a piezoresistive pressure sensor, the output of the sensor is sensitive to the change in the temperature due to the thermal expansion of the diaphragm [59-60]. Therefore, we consider beneficial to study the effect of the temperature on the response of the developed ICP monitoring system. For this purpose, the same measurement setup is used as explained in Section 4.3.1. Only difference is

that we take pressure readout measurements at four different temperatures. Figure 42 shows the received signal frequency from the implant for different temperature and pressure values. We can conclude as following [Publication VII]:

(i) The frequency of the received signal from the implant shifts to lower value with the increase of the temperature.
(ii) The pressure readout response of the system remains linear.
(iii) There is 7 $mmHg$ error in pressure readout per $1°C$ change in the temperature.

This indicates that temperature variation has significant effect on the pressure readout accuracy. However, this error can be removed by using a piezoresistive pressure sensor with build in temperature compensation or by monitoring the body temperature along with the pressure measurement.

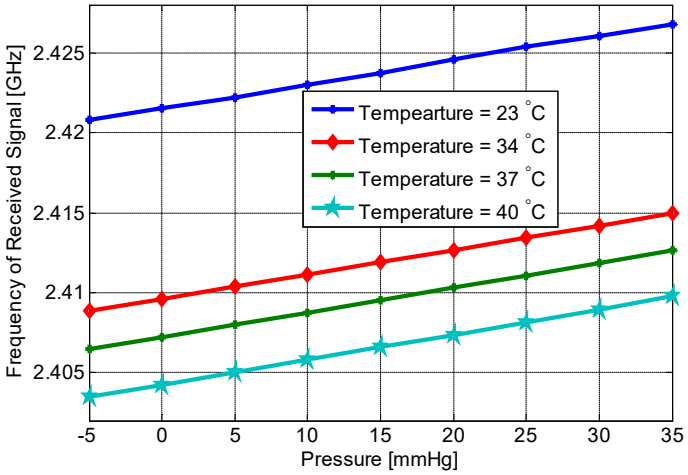

Figure 42. Received frequency of the implant signal at different pressure and temperature values [Publication VII].

6 Conclusions

In this work, we present the simulation and the measurement results of an inductively powered implantable system with targeted application of the intracranial pressure (ICP) monitoring. The system has three main parts: implant, on-body unit and off-body unit. The near-field inductive powering successfully activates the implant. The designing, simulation and measurement results from the inductive near-field link show that on-body unit antenna activates the implant without violating the SAR limit.

The developed system shows an accuracy of $1\ mmHg$ in the air and in the water when a data transmission unit is not included in the implant. However, with the inclusion of the data transmission unit in the implant, the system accuracy drops to $2\ mmHg$. The developed system response in a setting mimicking the human head environment proves the system operational capability.

The implant coating not only provides the desired biocompatibility but also helps to improve the inductive near-field link efficiency and gain of the far-field antenna. Initially, for misaligned cases, the system showed poor response with the 2-turns loop antenna of the on-body unit. However, with newly proposed 3-D loop antenna of the on-body unit significantly reduces the pressure readout error of the system due to misalignment between the coupled antennas. There is maximum $9\ mmHg$ improvement in the pressure readout with the 3-D loop antenna of the on-body unit. Moreover, the experiment results indicate that the response of the ICP monitoring system is significantly affected with the change in temperature. This puts the requirement to monitor the body temperature along with the ICP for accurate measurement.

6.1 Future Trends

As concluded in Section 5.2 that temperature change significantly affects the system response. Therefore using a piezoresistive sensor with build in temperature compensation feature can help to solve this problem. Another solution is to use the capacitive pressure sensor, which is less affected with the change in the temperature. However, using a capacitive pressure sensor will require more changes in the implant circuitry.

Although the system is tested in a setting that accurately model the human head environment, however, testing the system in real environment (*in-vivo test*) can be a future step.

Although we are able to activate the implant within the SAR regulation. However, it is believed that low power electronics or system on chip concept could improve further the implant in terms of the power consumption. Usage of piezoresistive pressure sensor with high input impedance could also reduce the implant power consumption.

References

[1] B. Mokri, “The Monro-Kellie hypothesis: applications in CSF volume depletion,” *Neurology*, vol. 56, no. 12, pp. 1746–1748, 2001.

[2] G. Kellie, “Appearances observed in the dissection of two individuals; death from cold and congestion of the brain,” *Transactions of the Medico-Chirurgical Society of Edinburgh*, vol. 1, article 84, 1824.

[3] F. Magendie, “*Recherches anatomique et physiologique sur leiquide cephalo-rachidien ou cerebro-spinal*,” Paris, France,1842.

[4] G. Burrows, *On Disorders of the Cerebral Circulation and on the Connection between Affections of the Brain and Diseases of the Heart, Lea & Blanchard*, Philadelphia, Pa, USA, 1848.

[5] Stephan A. Mayer and Ji Y. Chong, “Critical care management of increased intracranial pressure,” *J. Intensive Care Med*., vol. 17, no. 2, pp. 55–67, 2002.

[6] M. Smith, “Monitoring intracranial pressure in traumatic brain injury,” *Anesth. Analg*., vol. 106, no. 1, pp. 240–248, 2008.

[7] L. Rangel-Castillo, S. Gopinath and C. S. Robertson, “Management of intracranial hypertension,” *Neurol. Clin*., vol. 26, no. 2, pp. 521–541, 2008.

[8] R. Jalan, S. W. Olde Damink, N. E. P. Deutz, A. Lee and P. C. Hayes, “Moderate hypothermia for uncontrolled intracranial hypertension in acute liver failure,” *Lancet*, vol. 254, no. 9185, pp. 1164–1168, 1999.

[9] R. Beer, P. Lackner, B. Pfausler and E. Schmutzhard, “Nosocomial ventriculitis and meningitis in neurocritical care patients,” *J. Neurol*., vol. 255, no. 11, pp. 1617–1624, 2008.

[10] D. I. Friedman and D. M. Jacobson, “Diagnostic criteria for idiopathic intracranial hypertension,” *Neurology*, vol. 59, no. 10, pp. 1492–1495, 2002.

[11] Headsense, “Headsense,” http://www.head-sense-med.com/. [Site accessed on 25.12.2017]

[12] F. M. Kashif, G. C. Verghese, V. Novak, M. Czosnyka and T. Heldt. “Model-based noninvasive estimation of intracranial pressure from cerebral blood flow velocity and arterial pressure,” *Sci Transl Med* 4: 129ra44, Apr. 2012

[13] P. H. Raboel, J. Bartek, M. Andresen, B. M. Bellander and B. Romner, “Intracranial pressure monitoring: invasive versus non-invasive methods – a review,” *Crit. Care Res. Pract*., vol. 2012, article ID: 950393, Mar. 2012.

[14] U. Kawoos, M.-R. Tofighi, R. Warty, F. A. Kralick and A. Rosen, “In-vitro and in-vivo trans-scalp evaluation of an intracranial pressure implant at 2.4 GHz,” *IEEE Trans. Microw. Theory Techn.*, vol. 56, no. 10, pp. 2356–2365, Oct. 2008

[15] K. Aquilina, M. Thoresen, E. Chakkarapani, I. K. Pople, H. B. Coakham and R. J. Edwards, “Preliminary evaluation of a novel intraparenchymal capacitive intracranial pressure monitor: Laboratory investigation,” *J. Neurosurg*., vol. 115, no. 3, pp. 561–569, 2011.

[16] L. Y. Chen, B. C. K. Tee, A. L. Chortos et al., “Continuous wireless pressure monitoring and mapping with ultra-small passive sensors for health monitoring and critical care,” *Nature Commun*., vol. 5, article 5028, 2014.

[17] Mohammad H. Behfar, E. Moradi, T. Björninen, L. Sydänheimo and L. Ukkonen, “Biotelemetric wireless intracranial pressure monitoring: an in vitro study*,” Intl. J. Antennas and Propag.*, vol. 2015, article ID 918698, 10 pages, 2015.

[18] A. K. RamRakhyani, S. Mirabbasi and M. Chiao, “Design and optimization of resonance-based efficient wireless power delivery systems for biomedical implants,” *IEEE Trans. Biomed. Circuits. Syst*., vol. 5, no. 1, pp. 48–63, Feb. 2011.

[19] Constantine A. Balanis, “*Antenna Theory: Analysis and Design*,” 3rd ed., John Wiley & Sons, Inc., 2005.

[20] A. Kiourti, M. Christopoulou and K. S. Nikita, “Performance of a novel miniature antenna implanted in the human head for wireless biotelemetry,” *IEEE AP-S/URSI*, pp. 392-395, 2011.

[21] A. Kiourti and K. S. Nikita, “Miniature scalp-implantable antennas for telemetry in the MICS and ISM bands: design, safety considerations and link budget analysis,” *IEEE Trans. Antennas Propag*., vol. 60, no. 8, pp. 3568-3575, 2012.

[22] T. F. Chien, C. M. Cheng, H. C. Yang, J. W. Jiang and C. H. Luo, “Development of nonsuperstrate implantable low-profile CPW-fed ceramic antennas,” *IEEE Antennas Wireless Propag. Lett.,* vol. 9, pp. 599-602, 2010.

[23] P. Soontornpipit, C. M. Furse and You Chung Chung, “Miniaturized biocompatible microstrip antenna using genetic algorithm,” *IEEE Trans. Antennas Propag*., vol. 53, no. 6, pp. 1939-1945, 2005.

[24] C. Liu, Y. X. Guo and S. Xiao, “A hybrid patch/slot implantable antenna for biotelemetry devices,” *IEEE Antennas Wireless Propag. Lett*., vol. 11, pp. 1646-1649, 2012.

[25] I. Gani and H. Yoo, “Multi-band antenna system for skin implant,” *IEEE Microwave and Wireless Components Letters*, vol. 26, no. 4, pp. 294-296, 2016.

[26] L. J. Xu, Y. X. Guo and W. Wu, “Dual-band implantable antenna with open-end slots on ground,” *IEEE Antennas Wireless Propag. Lett.,* vol. 11, pp. 1564-1567, 2012.

[27] P. Soontornpipit, C. M. Furse and Y. C. Chung, “Design of implantable microstrip antenna for communication with medical implants,” *IEEE Trans. Microw. Theory Techn.*, vol. 52, no. 8, pp. 1944-1951, 2004.

[28] J. Kim and Y. Rahmat-Samii, “Implanted antennas inside a human body: simulations, designs, and characterizations,” *IEEE Trans. Microw. Theory Techn.,* vol. 52, no. 8, pp. 1934–1943, 2004.

[29] R. Warty, M. R. Tofighi, U. Kawoos and A. Rosen, “Characterization of implantable antennas for intracranial pressure monitoring: reflection by and transmission through a scalp phantom,” *IEEE Trans. Microw. Theory Techn.,* vol. 56, no. 10, pp. 2366–2376, 2008.

[30] C. Liu, Y. X. Guo and S. Xiao, “Compact dual-band antenna for implantable devices,” *IEEE Antennas Wireless Propag. Lett*., vol. 11, pp. 1508-1511, 2012.

[31] T. Karacolak, A. Z. Hood and E. Topsakal, “Design of a dual-band implantable antenna and development of skin mimicking gels for continuous glucose monitoring,” *IEEE Trans. Microw. Theory Techn.,* vol. 56, no. 4, pp. 1001–1008, 2008.

[32] C. M. Lee, T. C. Yo, C. H. Luo, C. H. Tu and Y. Z. Juang, “Compact broadband stacked implantable antenna for biotelemetry with medical devices,” *Electron. Lett.*, vol. 43, no. 12, pp. 660-662, 2007.

[33] W. C. Liu, S. H. Chen and C. M. Wu, “Implantable broadband circular stacked PIFA antenna for biotelemetry communication,” *J. Electromagn. Waves Appl*., vol. 22, no. 13, pp. 1791-1800, 2008.

[34] W. C. Liu, S. H. Chen and C. M. Wu, “Bandwidth enhancement and size reduction of an implantable PIFA antenna for biotelemetry devices,” *Microw. Opt. Technol. Lett.*, vol. 51, no. 3, pp. 755–757, 2009.

[35] L. J. Xu, Y. X. Guo and W. Wu, “Miniaturized dual-band antenna for implantable wireless communications,” *IEEE Antennas Wireless Propag. Lett.,* vol. 13, pp. 1160-1163, 2014.

[36] L. J. Xu, Y. X. Guo and W. Wu, “Bandwidth enhancement of an implantable antenna,” *IEEE Antennas Wireless Propag. Lett.,* vol. 14, pp. 1510-1513, 2015.

[37] C. Liu, Y. X. Guo and S. Xiao, “Capacitively loaded circularly polarized implantable patch antenna for ISM band biomedical applications,” *IEEE Trans. Antennas Propag.*, vol. 62, no. 5, pp. 2407–2417, 2014.

[38] C. J. Sanchez-Fernandez, O. Quevedo-Teruel, J. Requena-Carrion, L. Inclan-Sanchez and E. Rajo-Iglesias, “Dual-band microstrip patch antenna based on short-circuited ring and spiral resonators for implantable medical devices.” *IET Microwaves, Antennas Propag*., vol. 4, no. 8, pp. 1048-1055, 2010.

[39] Simon R. Saunders and Alejandro Aragon-zavala, *"Antennas and propagation for wireless communication systems,"* 2nd edition, 2007.

[40] R. sarpeshkaar, "*Ultra low power bioelectronics*," Cambridge University Press, USA, 2010.

[41] E. Moradi, T. Björninen, L. Sydänheimo, L. Ukkonen and J. M. Rabaey, "Analysis of wireless powering of mm-size neural recording tags in RFID-inspired wireless brain-machine interface systems," *IEEE RFID Conf.,* Orlando, FL, USA, pp. 8–15, May 2013.

[42] G. J. Hayes, J. H. So, A. Qusba, M. D. Dickey and G. Lazzi, "Flexible liquid metal alloy (EGaIn) microstrip patch antenna," *IEEE Trans. Antennas Propag*., vol. 60, no. 5, pp. 2151–2156, 2012.

[43] C. P. Lin, C. H. Chang, Y. T. Cheng and C. F. Jou, "Development of a flexible SU-8/PDMS-based antenna," *IEEE Antennas Wireless Propag. Lett.,* vol. 10, pp. 1108–1111, 2011.

[44] H. R. Khaleel, H. M. Al-Rizzo, D. G. Rucker and S. Mohan, "A compact polyimide based UWB antenna for flexible electronics," *IEEE Antennas Wireless Propag. Lett*., vol. 11, pp. 564–567, 2012.

[45] T. Kellomäki and W. G. Whittow, "Bendable plaster antenna for 2.45 GHz applications," *in Proc. LAPC*, pp. 453–456, 2009

[46] Y. Qiu et al., "Compact parylene-c-coated flexible antenna for WLAN and upper-band UWB applications," *Electron. Lett*., vol. 50, no. 24, pp.1782–1784, 2014.

[47] Y. H. Jung et al., "A Compact parylene-coated WLAN flexible antenna for implantable electronics," *IEEE Antennas Wireless Propag. Lett*., vol. 15, pp. 1382-1385, 2016.

[48] H. Lin, M. Takahashi, K. Saito and K. Ito, "Performance of implantable folded dipole antenna for in-body wireless communication," *IEEE Trans. Antennas Propag.*, vol. 61, no. 3, pp. 1363–1370, 2013.

[49] S. Bakogianni and S. Koulouridis, "An implantable planar dipole antenna for wireless MedRadio-Band biotelemetry devices," *IEEE Antennas Wireless Propag. Lett*., vol. 15, pp. 234-237, 2016.

[50] M. Mark, T. Björninen, Y. D. Chen, S. Venkatraman, L. Ukkonen, L. Sydänheimo, J. M. Carmena and J. M. Rabaey,. "Wireless channel characterization for mm-size neural implants," *IEEE EMBS*, pp. 1565–1568, Aug. 2010.

[51] S. Gabriel, R. W. Lau and C. Gabriel, "The dielectric properties of biological tissues: III. parametric models for the dielectric spectrum of tissues," *Phys. Med. Biol*., vol. 41, no. 11, pp. 2271–2293, Nov. 1996.

[52] G. Hartsgrove, A. Kraszewski and A. Surowiec, “Simulated biological materials for electromagnetic radiation absorption studies,” *Bioelectromagn.*, vol. 8, no. 1, pp. 29–36, 1987.

[53] F. C. Flack, E. D. James and D. M. Schlapp, “Mutual inductance of air-cored coils: Effect on design of radio-frequency coupled implants,” *Med. Biol. Eng. Comput*. , vol. 9, pp. 79–85, 1971.

[54] E. S. Hochmair, “System optimization for improved accuracy in transcutaneous signal and power transmission,” *IEEE Trans. Biomed. Eng*., vol. BME-31, no. 2, pp. 177–186, 1984.

[55] M. Soma, C. D. Galbraith and R. White, “Radio-frequency coils in implantable devices: misalignment analysis and design procedure,” *IEEE Trans. Biomed. Eng.,* vol. BME-34, no. 4, pp. 276–282, 1987.

[56] S. Babic and C. Akyel, “Improvement in calculation of the self- and mutual inductance of thin-wall solenoids and disk coils,” *IEEE Trans. Magn*. , vol. 36, no. 4, pp. 1970–1975, Jul. 2000.

[57] S. Babic and C. Akyel, “Calculating mutual inductance between circular coils with inclined axes in air,” *IEEE Trans. Magn.*, vol. 44, no. 7, pp. 1743–1750, Jul. 2008.

[58] K. Fotopoulou and B. W. Flynn, "Wireless power transfer in loosely coupled links: coil misalignment model," *IEEE Transactions on Magnetics*, vol. 47, no. 2, pp. 416-430, Feb. 2011.

[59] S.-C. Kim, K. D. Wise and W.-K. Chen, “Temperature sensitivity in silicon piezoresistive pressure transducers,” *IEEE Trans. Electron. Dev*., vol. 30, no. 7, pp. 802¬¬–810, July 1983.

[60] U. Aljancic, D. Resnik, D. Vrtacnik, M. Mozek and S. Amon, “Temperature effects modeling in silicon piezoresistive pressure sensor,” *IEEE Mediterranean Electrotechnical Conference*, pp. 36–40, 2002.

Tampereen teknillinen yliopisto
PL 527
33101 Tampere

Tampere University of Technology
P.O.B. 527
FI-33101 Tampere, Finland

ISBN 978-952-15-4152-0
ISSN 1459-2045